Design and construction of system for ultrafast ultraviolet-blue pump-probe exposure of biological samples.

A Thesis, Presented

by

Daniel Arthur Flickinger

to

The Graduate School

in Partial Fulfillment of the

Requirements

for the Degree of

Master of Science

in

Physics

Scientific Instrumentation

Stony Brook University

December 2005

Stony Brook University

The Graduate School

Daniel Arthur Flickinger

We, the thesis committee for the above candidate for the Master of Science degree, hereby recommend acceptance of this thesis.

Thomas Weinacht
Assistant Professor, Department of Physics & Astronomy
Thesis Advisor

Chris Jacobsen
Professor, Department of Physics & Astronomy

Michael Rijssenbeek
Professor, Department of Physics & Astronomy

Janet Hearing
Assistant Professor, Department of Molecular Genetics & Microbiology

This thesis is accepted by the Graduate School.

Dean of the Graduate School

Abstract of the Thesis

Design and construction of system for ultrafast ultraviolet-blue pump-probe exposure of biological samples.

by

Daniel Arthur Flickinger

Master of Science

in

Physics

Scientific Instrumentation

Stony Brook University

2005

We have created a device which produces a beam of intense, ultrafast blue and ultraviolet laser pulses with many controllable parameters, and uses these to irradiate a small-volume, liquid-phase, recoverable biological sample. This device consists of a preexisting amplified, ultrafast, infrared laser, and several newly created sub-systems: a nonlinear optical frequency conversion system, a bichromatic prism pair interferometer, and two pulse characterization systems. One experiment was undertaken to verify the functionality of this device using the pulse characterization systems, and an ongoing series of experiments tested the suitability

of the device for covalently crosslinking DNA to DNA-binding proteins in solution. Results of these experiments will be given.

To my Father and Mother.

Contents

List of Figures

List of Tables

Acknowledgements

It has been my great pleasure to work in the laboratory of Professor Thomas Weinacht and to work closely with him and Professor Janet Hearing on this thesis project. They both deserve tremendous credit for this work and for the success that I have found at Stony Brook, and not only because of their obviously ample scientific knowledge and skills. I was lucky to receive two equally warm and kind advisers who were admirably generous with their time and help when needed, and who were a pleasure to work with as well.

I would like to thank David Cardoza, Carlos Trallero, Sarah Nichols, and Brett Pearson for their role in making my time here enjoyable and productive. They were all helpful when needed, whether it was for fixing a cranky laser, lending a book, or pointing me towards the nearest source of free food. And I can't imagine any other set of "labmates" being able to make a three hour group meeting not only bearable, but fun!

Looking to the previous year I have to thank my minor project advisor Chris Jacobsen for the time, resources, and guidance that he provided (not to mention the turkey too!). Holger Fleckenstein, Mirna Lerotic, Bjorg Larson, Benjamin Hornberger, and especially Sue Wirick are memorable for their help and general friendliness during these days. I hope to see them, and

those already mentioned, again and often as long as I'm here on the Island.

I need to thank my parents for the immense amount of support and love that they have given me, and for showing so much trust in my decisions, even as they have led me many miles farther away from them than any of us can be happy with. This milestone is theirs as much as it is my own.

Finally, I would like to thank Meg for her love and companionship throughout this past year. We first met when this project began, and I am very glad that we will continue on even as my time at Stony Brook comes to a close.

Daniel Arthur Flickinger

Stony Brook, New York

December 2005

Chapter 1

Introduction

Ultrafast optical science is the study of phenomena that occur on time scales less than ~ 1 picosecond (1 ps = 10^{-12} s), using light pulses that are themselves shorter than the length of the phenomena being studied. Thanks to a series of advances in laser science that have taken place over decades [13], ultrafast laser pulses on the order of 100 femtosecond long (1 fs = 10^{-15} s) are now routinely available in turn-key systems, while shorter pulses (10-30 fs) are available to those willing and able to dedicate some time and money to understanding and caring for both the lasers that produce them [2] and for the specialized optics necessary to keep them short [22]. The most dedicated and meticulous workers produce optical pulses that are shorter than 10 fs (which contain no more than 2 or 3 optical cycles each!) [7] and UV/XUV pulses that are measured in the hundreds of attoseconds (10^{-18} s) [1].

Along with these short time scales comes the possibility of producing enormous energy densities. Femtosecond-length pulses are usually created with mode-locked Ti:Sapphire lasers, and at this stage the energy per pulse is limited to the nanojoule range. Pulse amplification systems currently

exist, however, that allow these pulses to be amplified by factors of 10^6 or more, while only negligibly affecting their lengths. Powers for these pulses can reach terawatt (10^{12} W) levels in small laboratories, and more in larger facilities. The review articles [2, 13, 4] provide excellent details about the lasers and amplifiers used to produce these pulses. By focusing pulses with these energies to the smallest possible spots, light intensities of 10^{20} W cm^{-2} can be produced, which, according to [2] is an "intensity greater than that which would be obtained by focusing the entire solar flux incident on the earth, onto a pinhead."

Many types of physical phenomenon can be explored using these laser pulses, from the dynamics of electrons in atoms and molecules to inertial confinement fusion. In our laboratory specifically, we produce amplified, 30 fs laser pulses with energies of 1 mJ each and use them primarily to study the dynamics of atomic and molecular systems by shaping the pulses with closed-loop learning control [8]. This is certainly an interesting topic, but is not the focus of this thesis.

The specific catalyst for this journey into the world of ultrafast optical science was an application of importance to molecular genetics—the photochemical crosslinking of DNA to DNA-binding proteins. This crosslinking process is an important step in many molecular genetic studies of the protein-DNA interaction, and is detailed in Chapter 5. Interestingly, it could not be said that this process *requires* femtosecond-length pulses and the high intensities available with amplified lasers. However, evidence suggested that it could possibly benefit from them, and the fact that the project was under-

taken at all reflects the *relative* ease with which these intense ultrafast pulses can now be obtained.

The basic requirement for this crosslinking project was to have the ability to expose a DNA and protein mix in solution to a series of femtosecond-length ultraviolet and blue pulses while having control over the delays between these pulses. The devices that we have built make this possible, and allow another important type of control over the blue and UV pulses that will be discussed.

At this time, only a moderate amount of success has been achieved towards the goal of producing efficient DNA-protein crosslinking with the laser system that is available to us, and consequently it is not yet known whether this work will be of much interest to the molecular genetics community. Along with this bad news, however, comes the good news that the central device built to perform this crosslinking—which we call the bichromatic prism pair interferometer (BPPI)—is itself novel and potentially useful for this and many other applications. For this reason, we have verified and characterized the performance of the BPPI in order both to rule it out as the source of our sub-optimal crosslinking results, and to be able to present it to a potentially interested ultrafast optics community. This work has been successful, and will comprise the bulk of this thesis.

Chapter 2

Theory Background

A brief mathematical treatment of concepts in two main areas that are important to this thesis will be presented. The first area is ultrafast pulse propagation and dispersion, and the second is non-linear optical frequency generation.

2.1 Ultrafast pulse propagation

There are a few important simplifications used throughout this thesis. The first is that all pulses considered can be represented as the product of temporal and spatial components, which allows one to disregard the spatial extent of the pulses in the mathematical treatment of most interactions. This condition will remain true if there is no coupling between the time and transverse spatial domains of the pulses during their propagation through an optical system (in other words, all frequency components of the pulses are imaged in the same way), which is a condition that we and most workers in ultrafast laser research strive to maintain. To be clear, individual optical components

such as prisms *have* been used exactly because they *cause* this coupling to occur, but these components have been arranged together and carefully aligned such that a beam, when traveling through the set of them, experiences no overall coupling, and a beam that is separable into temporal and spatial components upstream of the set will be separable downstream of it.

The second simplification is that all pulses are linearly polarized, and that the polarization direction is either s or p. Often, the polarization direction does not matter, and it is only necessary to consider the scalar component of the electric field. In almost all cases, it is only necessary to consider the scalar component along with the s- or p-polarization direction. Like with the space-time coupling simplification above, maintaining the polarization of the beam such that this simplification is possible is of great importance in our laboratory, and any measured deviation from this condition is diagnosed and corrected.

The third simplification is the slowly varying envelope approximation, which if valid allows the electric field of a pulse to be written as a product of an oscillator and a relatively slowly varying amplitude envelope function:

$$E(t) = A(t) \exp[i\phi(t)] \ , \tag{2.1}$$

where $A(t)$ is an envelope function that does not vary appreciably over one optical cycle. In this general case, optical cycles happen at the speed of the instantaneous angular frequency

$$\omega(t) = \frac{d\phi}{dt} \ . \tag{2.2}$$

If the slowly varying amplitude approximation is valid, then we know that we can write a very useful expression for the cycle averaged electric field irradiance

$$I(t) = \frac{1}{2}\epsilon_0 cnA(t)^2 \ , \tag{2.3}$$

where ϵ_0 is the standard vacuum permitivity, c is the speed of light, and n is the refractive index of the medium that the fields exist in.

Also very useful will be the frequency domain representation of the electric field,

$$\tilde{E}(\omega) = \int E(t)\exp(i\omega t)\ dt = \tilde{A}(\omega)\exp(i\tilde{\phi}(\omega)) \ , \tag{2.4}$$

where $\tilde{E}(\omega)$ is the Fourier transform of $E(t)$, $\tilde{A}^2(\omega)$ gives the power spectrum of the pulse, and $\tilde{\phi}(\omega)$ is the spectral phase.

2.1.1 Group velocity dispersion

Short laser pulses necessarily have a large bandwidth. Fourier transform theory applied to $\tilde{A}(\omega)$ and $A(t)$ can be used to prove this. If one defines the FWHM width of the power spectrum $\tilde{A}^2(\omega)$ as $\Delta\omega = 2\pi\Delta f$ and defines the FWHM width of the pulse intensity in time as Δt, then this fact is manifested in the time-bandwidth product relationship

$$\Delta f \Delta t \geq c_B \ , \tag{2.5}$$

where c_B is a constant of the order of unity that depends on the particular pulse shapes involved (for Gaussian pulses, $c_B = 0.44$, which is particularly small). The term "transform-limited" refers to pulses for which the right

and left hand sides of eq. 2.5 are equal, and thus they are the shortest pulses possible for a given bandwidth. One can see that as transform-limited pulses get shorter, their bandwidths must become larger. Because of this, dispersion in optical systems that are used with ultrashort pulses must be seriously considered.

To a first order approximation, we can model pulse propagation through an optical system using the spectral transfer function $\tilde{S}(\omega)$ as [22]

$$\tilde{E}_{\text{out}}(\omega) = \tilde{S}(\omega)\tilde{E}_{\text{in}}(\omega) \ . \tag{2.6}$$

The argument of the spectral transfer function is the spectral phase transfer function $\varphi(\omega)$. This function gives the phase that is accumulated by each spectral component of the pulse upon propagation between the two reference planes that bound the optical system in question.

To simplify the examination of the effect of an optical system with dispersion on pulses, $\varphi(\omega)$ is usually written as a Taylor expansion around the central frequency of the pulse ω_0:

$$\varphi(\omega) = \sum_n \frac{1}{n!}\varphi^{(n)}(\omega_0)(\omega - \omega_0) \ . \tag{2.7}$$

The values of $\varphi^{(n)}(\omega_0)$, which are usually stated in units of [fs^n] are then used to describe the system response, although usually one or two of them contain all of the required information. The zero-th derivative gives an absolute phase accumulated at the reference frequency ω_0, and the first derivative, which is known as the group delay, is simply the time that it takes the pulse

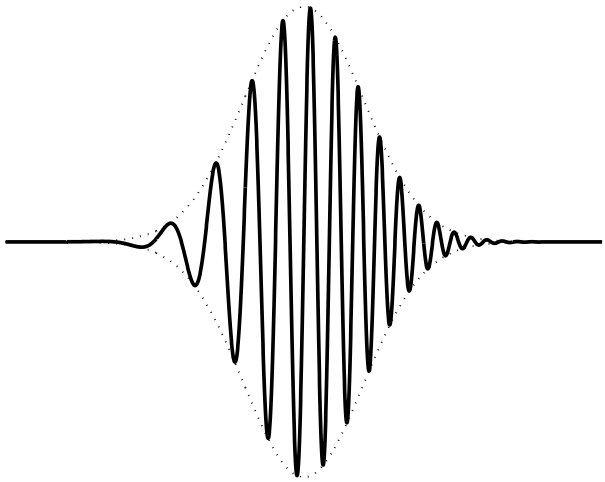

Figure 2.1: Example of chirped Gaussian pulse, showing Gaussian envelope.

envelope to travel between the reference planes. Neither are important for pulse shape.

The second derivative $\varphi^{(2)}(\omega_0)$ is known as the group velocity dispersion (GVD), and it is the most important propagation parameter for ultrashort pulses. It can be thought of as the rate of change (as a function of frequency) of the group velocities of the different spectral components of the pulse. If it is non-zero for a system, the result is that different spectral components take different amounts of time to traverse that system, and thus these different components separate from each other within the pulse. The resulting pulse is broadened in time, and is said to be "linearly chirped" (Fig. 2.1), which reflects the fact that it has an instantaneous frequency (eq. 2.2) that varies linearly with time:

$$\omega_{\text{chirped}}(t) = \omega_0 + bt \ . \tag{2.8}$$

The next higher order dispersion terms are known as third order dispersion (TOD), fourth order dispersion (FOD), and so on. These terms have progressively less pronounced effects on pulse propagation, and are usually only considered when designing ultrafast lasers and analyzing the propagation of pulses < 30 fs long.

As a concrete example of pulse broadening, one can consider Gaussian pulses, which are used extensively in modeling ultrafast systems due to their mathematical tractability and close approximation to nature in many circumstances. For a transform limited Gaussian pulse that is described by

$$E(t) = \exp\left(-\frac{2\ln 2}{\Delta t^2}\ t^2\right) \exp i(\omega_0 t + bt^2)\ , \tag{2.9}$$

the linear chirp is parameterized by b. If b is initially zero, this means that the pulse is initially transform limited. If b is positive or negative, then the pulse will be positively or negatively chirped. When passing through a system with $GVD \equiv \varphi^{(2)}(\omega_0)$, an initially transform limited pulse will by stretched to a chirped pulse with FWHM equal to [22]

$$\Delta t_{\text{out}} = \Delta t_{\text{in}} \sqrt{1 + \frac{16(\ln 2)^2\ [\phi^{(2)}(\omega_0)]^2}{\Delta t_{\text{in}}^4}}\ . \tag{2.10}$$

As one can see, the shorter the pulse is to begin with, the more it is relatively stretched. This can be intuitively understood because shorter transform-limited pulses have more bandwidth, and thus there are more frequency components present that will experience greater relative delays.

2.1.2 Sources of GVD

For propagation through a material with thickness $\mathcal{D}$ and index of refraction $n(\omega)$, the spectral phase advance is given by

$$\varphi(\omega) = \frac{\omega}{c} n(\omega) \mathcal{D} \ , \tag{2.11}$$

and GVD can thus be calculated

$$\mathrm{GVD}_{\mathrm{mat}}(\omega) = \frac{d^2\varphi}{d\omega^2} = \frac{\mathcal{D}}{c}\left(\omega\frac{d^2n}{d\omega^2} + 2\frac{dn}{d\omega}\right) = \mathcal{D}\left(\frac{\lambda^3}{2\pi c^2}\right)\frac{d^2n}{d\lambda^2} \ . \tag{2.12}$$

For most transparent materials in the optical region, $d^2n/d\lambda^2$ is positive, and thus most transparent materials have a positive value of GVD.

If one wants to propagate ultrashort pulses through transparent material and maintain their temporal structure, optical elements that exhibit negative GVD must be used. Such elements can be adjusted to provide negative GVD that exactly cancels positive GVD that is present in a system, such that transform limited pulses that enter the system remain transform limited at exit (as long as higher order dispersions are negligible). Terms commonly used for this technique include "compression" if the negative GVD comes after the pulses are positively chirped and "precompensation" if the negative GVD comes before the positive, such that they are negatively chirped first, and then the positive GVD material compresses them back to a shorter state.

Fortunately, such negative GVD devices can be implemented relatively simply through the use of angular dispersion and a suitable geometrical arrangement. Fig. 2.2 shows the general layout of a prism pair compres-

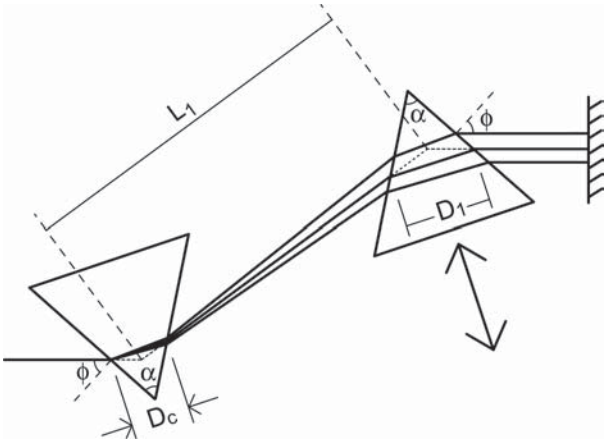

Figure 2.2: Layout of prism pair compressor, including definition of prism pair parameters, shown on one prism pair with rays representing the central, highest, and lowest frequency components of a beam.

sor (PPC) [5], which is a device that does just this. First order dispersion ($dn/d\lambda$) in the glass of the first PPC prism causes the different frequency components of the incoming beam (from the left in Fig. 2.2) to be sent through different paths in the device. Higher frequency components are refracted more by the first prism, and are thus made to travel through less material in the second prism than lower frequency components, which gives these higher frequency components a relative temporal advance. This temporal advance accounts for the negative GVD of the device. The second prism also exactly removes the angular dispersion caused by the first prism, but leaves the frequency components separated spatially. The retroreflection mirror causes the pulses to take the same path back through the PPC, which removes this spatial separation. Gratings are also commonly used to provide angular dispersion for geometrical negative GVD devices.

Prism pair compressors are especially useful for dispersion control because

they not only provide negative GVD through angular dispersion, but the prism material itself provides positive GVD that can be adjusted continuously and easily through moving the prisms along the direction perpendicular to their bases (Fig. 2.2). Adjusting this prism insertion does not steer the output beam at all and has no effect on the negative dispersion mechanism of the PPC because the same amount of material is added or removed from each frequency component passing through the prisms. Thus, by adjusting the prism insertion, the GVD of the PPC can be adjusted continuously from positive to negative values, through zero. The full expression for the GVD and higher order dispersions of a PPC are somewhat complicated (see [2] for expressions for 2–4th order dispersions for PPCs and grating compressors and [23] for a more precise derivation for PPCs), but to first order the GVD of a PPC is given by:

$$\mathrm{GVD}_{\mathrm{PPC}} \approx \frac{\lambda^3}{2\pi c^2}\left[\mathcal{D}\frac{d^2n}{d\lambda^2} - 4L\left(\frac{dn}{d\lambda}\right)^2\right]_{\lambda_0}, \tag{2.13}$$

where $\mathcal{D} = 2(D_c + D_1)$ is the mean total pathlength through the prism material on one round trip as seen in Fig. 2.2. One can see that the first term is the same as material GVD given by eq. 2.12, and that the negative GVD given by the second term is proportional to the separation between the prisms.

2.2 Nonlinear optical frequency generation

The second subject that will be treated in this chapter is nonlinear optical frequency generation (NOFG), which is a technique through which intense laser light of one or more central frequencies can be used to produce light with different central frequencies. It is a nonlinear optical technique because it makes use of the nonlinear polarizability of materials, which is only appreciable for high field amplitudes like those possible with ultrafast laser pulses. The apparatus that is used for NOFG is often not complex; a single crystal can be used in which pulses with a certain central frequency enter, and those pulses (having a reduced energy) exit along with pulses that have a different central frequency. However, the characteristics of the crystal have to be chosen carefully for efficient conversion to occur. Discussion of three basic types of NOFG and how to implement them are presented, prefaced by a brief review of the nonlinear polarization.

2.2.1 The nonlinear polarization

The classical treatment of EM waves traveling through polarizable material assumes that the polarization of the material varies linearly with the applied electric field. This is equivalent to

$$P = \epsilon_0 \chi E \ , \tag{2.14}$$

where χ is the electric susceptibility. For very high electric fields however, this relationship breaks down, and one can better understand the material

response by expressing the polarization as a series expansion in powers of E [6]:

$$P(t) = \epsilon_0(\chi E(t) + \chi_2 E^2(t) + \chi_3 E^3(t) + \ldots) \tag{2.15}$$

$$\equiv P_1(t) + P_2(t) + P_3(t) + \ldots \quad . \tag{2.16}$$

In general, E fields of course have a vector nature and the χ terms are tensors, but assuming a scalar nature for these quantities will not have a negative impact on the brief discussion here.

There are numerous consequences of this nonlinear polarizability. Second harmonic generation, sum frequency generation, and difference frequency generation, which all come from the second order term in eq. 2.16 will be discussed below. Third order effects such as third harmonic generation and the optical Kerr effect are also very important for ultrafast physics. The optical Kerr effect, in which the refractive index of a material is dependant on the applied optical field strength, is especially important for the production of ultrafast laser pulses and is used for several pulse characterization systems. The SD FROG system [21] and a self diffraction pulse characterization system built for this project rely on this effect. These systems are described in section 3.4.

2.2.2 Second order nonlinear optical effects

Imagine that a strong EM wave of the form

$$E = E_0 \sin \omega t \tag{2.17}$$

is incident on a medium. The electric polarization of the medium

$$P(t) = \epsilon_0 \chi E_0 \sin \omega t + \epsilon_0 \chi_2 E_0^2 \sin^2 \omega t + \epsilon_0 \chi_3 E_0^3 \sin^3 \omega t + \dots \tag{2.18}$$

can be written instead as [6]

$$P(t) = \epsilon_0 \chi E_0 \sin \omega t + \frac{\epsilon_0 \chi_2}{2} E_0^2 (1 - \cos 2\omega t) + \frac{\epsilon_0 \chi_3}{4} E_0^3 (3 \sin \omega t - \sin 3\omega t) + \dots \ . \tag{2.19}$$

Since the material polarization arises from the movement of charges within the material, an oscillating polarization creates EM radiation. The first, linear term produces the familiar refracted wave that has the same frequency as the incoming wave and travels with phase velocity $c/n \approx c/(1+\chi)^{\frac{1}{2}}$ through the material. The second term in eq. 2.19, however, contains $\cos 2\omega t$, which shows that the polarization is capable of radiating energy at the frequency 2ω, the second harmonic of the incident light. This is known as second harmonic generation, or SHG. Similarly, if two beams of different frequencies are incident on the material, then the polarization is given by substituting

$$E = E_{01} \sin \omega_1 t + E_{02} \sin \omega_2 t \tag{2.20}$$

into eq. 2.16. One finds that the second-order term in the polarization is

$$P_2(t) = \epsilon_0 \chi_2 (E_{01}^2 \sin^2 \omega_1 t + E_{02}^2 \sin^2 \omega_2 t + 2E_{01}E_{02} \sin \omega_1 t \sin \omega_2 t) \ , \quad (2.21)$$

and while the first two terms in eq. 2.21 can be transformed into functions of $2\omega_1 t$ and $2\omega_2 t$ like with the second term of eq. 2.18, the last term can be rewritten as

$$2E_{01}E_{02} \sin \omega_1 t \sin \omega_2 t = E_{01}E_{02} \left[\cos(\omega_1 - \omega_2)t - \cos(\omega_1 + \omega_2)t\right] . \quad (2.22)$$

Therefore, the polarization will radiate EM waves with frequencies that are the sum and difference frequencies of the two incident lightwaves. These processes are known as sum frequency generation (SFG) and difference frequency generation (DFG).

2.2.3 Conditions for efficient SHG, SFG, and DFG

The generation of significant amounts of light from SHG, SFG, and DFG does not ubiquitously occur when strong laser fields are incident on materials, so there must be some conditions that have to be met for this generation to occur efficiently.

The first condition is that the material not be centrosymmetric, or in other words, have an inversion symmetry. For materials that are centrosymmetric, the scalar quantity χ_2 must be zero [11]. One can see that this is true by considering a strong DC electric field in centrosymmetric media, which causes the second order polarization $P_2 = \epsilon_0 \chi_2 E^2$ (from eq. 2.16) to develop.

In the centrosymmetric case, if the electric field direction is reversed, then the polarization should be reversed and have the same magnitude that it had before. Applying this reasoning causes one to arrive at the contradiction

$$-P_2 = \epsilon_0 \chi_2 (-E)^2 = P_2 \tag{2.23}$$

which can only be solved if χ_2 is zero. All liquids, gasses, and amorphous solids, and many crystals are centrosymmetric, so this severely limits the materials in which second-order nonlinear optical effects can take place. Of course, for non-centrosymmetric media, the tensor χ_2 must be used for analysis. The general theory of non-linear optical susceptibility required for this will not be developed here, but this theory is not necessary to understand the required conditions for generating light from second-order nonlinear effects that are discussed here. An understanding of these conditions itself is the crucial knowledge that must be communicated.

The next condition for efficient second-order NOFG is called "phase-matching". This condition basically requires that the light fields involved all travel at the proper phase velocities, such that light that is radiated at all points in the NOFG crystal medium along the propagation direction z adds constructively to light that was radiated previously. For SFG and DFG, which have three light fields having frequencies ω_1, ω_2, and $\omega_3 = \omega_1 + \omega_2$, this condition is [3]

$$k_1 + k_2 = k_3 \ , \tag{2.24}$$

or

$$n_1\omega_1 + n_2\omega_2 = n_3\omega_3 \ . \tag{2.25}$$

SHG, in which there are only two light fields (ω_1 and $\omega_2 = 2\omega_1$) involved, can be thought of as a special case of SFG in which the two added light fields have the same frequency. For SHG, the phasematching condition is $2n_1\omega_1 = n_2\omega_2 = n_2(2\omega_1)$, or $n_1 = n_2$. For normal materials, this phasematching condition can not be achieved due to the dependance of the refractive index on light frequency.

Phasematching, however, *is* possible through the use of birefringent crystals. Through properly orienting the crystal, it is possible to properly phasematch two or three light fields if their polarizations are different from one another. For SHG, there are only two parameters that must be adjusted to achieve phasematching, the angle θ between the unique birefringent crystal axis and the propagation direction of the light, and rotation of the crystal about this propagation axis, which changes the orientation of this crystal axis relative to the polarization of the incoming ω_1 light field. In SFG and DFG, the two incoming light fields either have to be polarized the same way (called type I phasematching), or perpendicular to each other (called type II), but then it is still only θ and the crystal roll that have to be adjusted to achieve phasematching, if phasematching is at all possible for the wavelengths involved and the properties of the crystal.

In practice, the light entering and exiting a birefringent crystal for NOFG should do so very close to normal incidence, so that refraction at the air-crystal interfaces doesn't angularly separate the different frequency compo-

nents. Thus crystals for NOFG must be cut such that the angle between the crystal axis and crystal face is $\pi/2 - \theta$. These crystals are custom ordered, and it is necessary to calculate the proper phase matching angle θ for each NOFG situation before doing so. These steps were taken for this project.

2.2.4 Phasematching limitations

One last topic should be briefly considered. Since phasematching, for a given value of θ, is only possible for two or three specific frequencies of light at a time, there is a problem with doing NOFG with ultrafast pulses. These pulses necessarily have large bandwidths (see sec. 2.1.1), and phasematching conditions for frequency components that are far from their central frequencies are not perfect. As stated above, phasematching is necessary so that light created in the NOFG crystal always adds constructively with light made in other parts of the crystal, so the effect of imperfect phasematching is that the length of the crystal over which efficient NOFG can occur is limited. The larger the difference between the value $k_1 + k_2$ and the value of k_3 (see eq. 2.24), the shorter the distance over which NOFG can occur without losing efficiency due to destructive interference.

There is in fact an inverse relationship between the length of a NOFG crystal and the bandwidth of the pulses that it can mix efficiently. If a crystal is too long, then light generation only occurs for a portion of the frequency components within the pulses being mixed, and as a result the bandwidth of the generated pulse is small and its length can be significantly longer than the lengths of the incoming pulses. However, if the crystal is too thin,

then the NOFG will suffer from unnecessary inefficiency. Therefore, crystal thickness must be carefully chosen when working with ultrashort < 100 fs pulses. Crystals between 100μm and 1 mm thick are often used.

Chapter 3

Devices

This project was possible because of the availability of our Kerr lens mode-locked Ti:Sapphire laser with a chirped-pulse, multipass amplifier. This system produces laser pulses at a repetition rate of 1 kHz that average ≈ 30 fs in length (FWHM), contain 1 mJ of energy each, and have a central wavelength of 780 nm. The pulses are near-transform-limited, and contain a bandwidth of $\approx$ 30 nm. Although significant time and effort were dedicated towards understanding the operating principles of this laser system and becoming competent with its use, adjustment, and troubleshooting, most details about it have no specific importance for this project, and will not be given here. For a detailed treatment of the laser, consult reference [11].

Once again, the original purpose of this project was to create a collinear beam containing femtosecond-length UV and blue pulses, with the delay between the two differently colored pulses being controllable to a resolution of ~ 10 fs. The system that was built to do this and also roughly characterize these pulses can be broken down into 4 pieces by functionality (Fig. 3.1): a nonlinear frequency conversion (NLF) device where the blue and UV pulsed

beams are created, the bichromatic prism pair interferometer (BPPI) where these pulses are manipulated, a difference frequency cross correlation setup (DFXC) used to characterize the interaction between the blue and UV pulses, and a self diffraction setup (SD) used to indicate when the widths of the pulses are minimized through adjustment of BPPI parameters.

Figure 3.2 shows the arrangement of pulses that the NLF and BPPI devices indeed produce. Each set of UV and blue pulses is separated by the laser repetition period of 1 ms, and the UV–blue delay τ is controllable with high resolution. The BPPI also has the ability to control the lengths of the UV and blue pulses ($\Delta t_{2\omega}$ and $\Delta t_{3\omega}$) through manipulation of the GVD that they encounter.

3.1 Nonlinear frequency conversion setup

The nonlinear frequency conversion setup uses nonlinear optical effects to convert a portion of the red beam light into light at its second and third harmonics. The red (ω), blue (2ω) and UV (3ω) pulses that result are collinear, or at least vary negligibly from collinearity. It does this using only two components which are both thin crystals made of beta barium borate (β-BaB_2O_4, usually called BBO). Blue pulses are created in the first crystal, and UV pulses are created in the second.

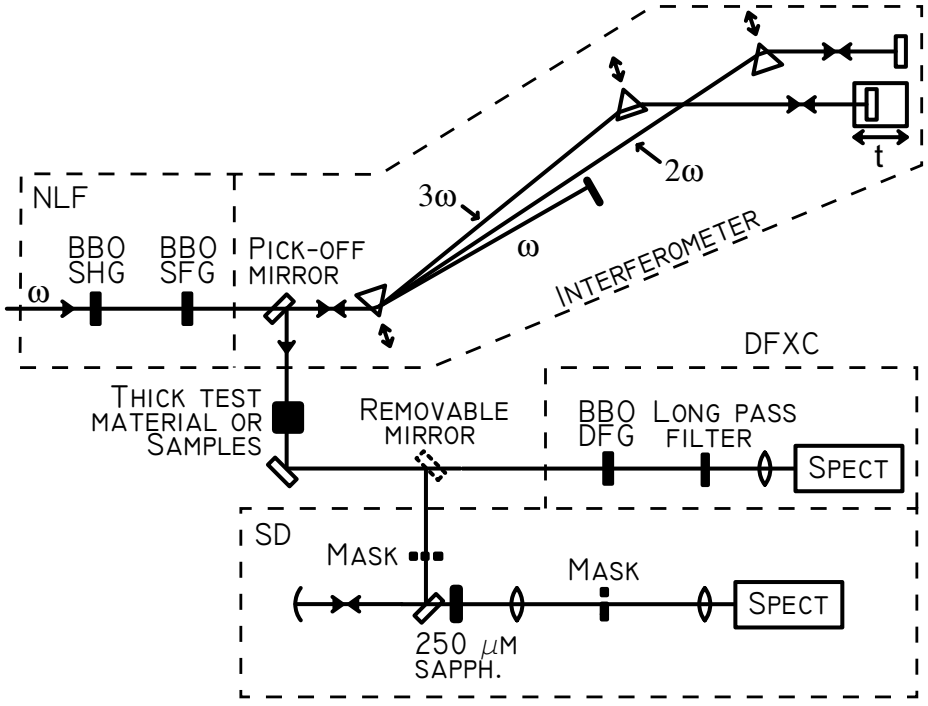

Figure 3.1: Overview of entire system. NLF – nonlinear frequency conversion setup, DFXC – difference frequency cross correlation setup, SD – self diffraction setup.

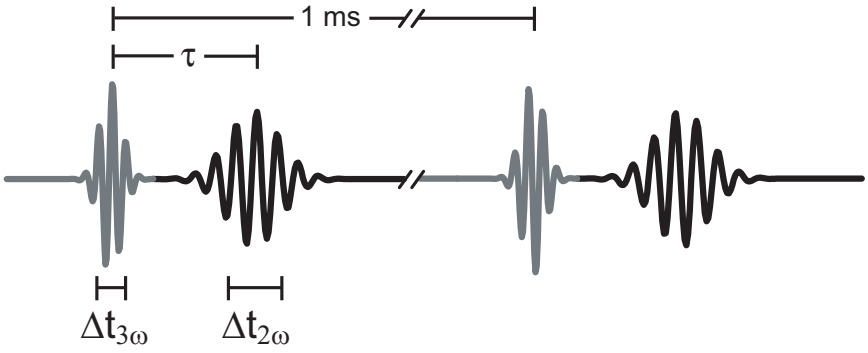

Figure 3.2: Cartoon of pulse train created by devices. Grey pulses represent UV light and black pulses represent blue.

3.1.1 Blue generation

In the first stage of the nonlinear frequency conversion, blue 390 nm pulses are made through SHG (see section 2.2.3). The BBO crystal used (from here labeled BBO_{SHG}) was custom ordered to be cut to phase-matching angle $\theta = 29.8°$. This is the angle for type I phase-matching of 780 nm and 390 nm light, as calculated using the SNLO software [18]. The dimensions of the crystal are $5 \times 5 \times 0.25$ mm, and the 5×5 mm area of the crystal that the beam can be sent through was constrained by price and is slightly smaller than the total, visible area of the red beam. Out of concern for safety, the red beam size is thus limited by an iris upstream of the BBO_{SHG} crystal in order to avoid scattering of the intense red light off of the crystal edges. The thickness of the crystal, which is often a crucial parameter for crystals used in non-linear optics, was chosen roughly to be as thick as possible without lengthening the blue pulse significantly through bandwidth limitations.

Currently, alignment of this crystal is done simply. After shining the red beam through the center of the crystal, the most important immediate concern is where the red and blue back-reflections off of the crystal surfaces (which do not have anti-reflection coatings) go. The yaw of the crystal is thus set to be as normal to the beam as possible, yet still direct these reflections onto a suitable block. This is not the best adjustment procedure if maximum conversion efficiency is the most important goal, but we easily received sufficient power in the blue beam for our experiments, so were willing to sacrifice some efficiency. The only other parameter needing adjustment is the roll of the crystal, which is changed until the maximum amount of blue

light is generated.

The conversion efficiency for blue production should depend linearly on red intensity [3]. The power of the red beam upon entering the NLF setup is usually $850-950$ mW, and in order to increase the efficiency of the harmonic generation, it was decided to increase the intensity of the red beam by down-collimating it using a non-focusing Galilean telescope. The maximum power observed in the resulting blue beam, during which the setup was optimized for generation of blue light, was ~ 120 mW. This is a reasonable conversion efficiency for this simple system. Usually, when the setup was optimized for the production of UV (see next section), the blue power was closer to ~ 50 mW. The reason or reasons why conditions for the maximum production of blue light and maximum production of UV light do not coincide are not precisely known, but are speculated on below.

We predict that the blue pulses will be longer than the red pulses, and that they will be delayed relative to the red as well. Both of these effects can be understood most easily as resulting from the different group velocities of 780 nm and 390 nm light in the BBO crystal. These group velocities can be easily found using the SNLO program, and the difference between them is called the group velocity mismatch (GVM). Because it makes it easier to understand the effect of the GVM, this quantity is not usually defined as $v_{\mathrm{g},\lambda_1} - v_{\mathrm{g},\lambda_2}$, but instead is defined

$$\mathrm{GVM}_{\lambda_1}^{\lambda_2} \equiv \frac{1}{v_{\mathrm{g},\lambda_2}} - \frac{1}{v_{\mathrm{g},\lambda_1}} \,. \tag{3.1}$$

For $\mathrm{BBO}_{\mathrm{SHG}}$, $\mathrm{GVM}_{780}^{390} \approx 200$ fs/mm, so if one imagines that two non-

interacting blue and red pulses enter the crystal coincident in time, then they will be separated by a delay of 200 fs for every mm of crystal that they pass through. One can define a "smear" for a particular crystal of thickness l to be

$$\mathrm{Sm}_{\lambda_1}^{\lambda_2} \equiv \mathrm{GVM}_{\lambda_1}^{\lambda_2}\, l\ , \tag{3.2}$$

and thus $\mathrm{Sm}_{780}^{390} \approx 50$ fs for $\mathrm{BBO_{SHG}}$. As the red pulse travels through this crystal, blue light is created spatially coincident with this pulse, but then the blue light lags behind the red as they travel. So, as they exit the crystal the blue pulse will be stretched in time relative to the length of the red, and the peak of the blue pulse will be delayed relative to the peak of the red. In order to estimate this delay and the blue pulse length, numerical simulations of the conversion were performed with SNLO and lab2 software [17]. Unfortunately, it was not easy to find good agreement between these models and to reproduce the conversion efficiencies seen experimentally. However, we were able to verify that this simple intuition about the effect of smear on the blue production is useful, and are confident that if the red pulse is 30 fs long that the length of the blue pulse is $35 - 50$ fs and that its peak is delayed by 5-20 fs after the red peak.

3.1.2 UV generation

UV light was created through sum frequency generation (SFG) of the red and blue light in a BBO crystal (labeled $\mathrm{BBO_{SFG}}$), and thus only occurred in the crystal where red and blue light were temporally overlapped. The red-to-blue delay present after $\mathrm{BBO_{SHG}}$ is therefore an important parameter

for generating UV efficiently. Often, delay compensation schemes using a bichromatic Mach-Zehnder interferometer are used to set this delay to zero, but we did not implement this due to cost constraints. The efficiency of our UV creation can be made to be sufficient without it.

The $\mathrm{BBO_{SFG}}$ crystal was ordered to have (type II) phase matching angle $\theta = 57.7°$, and had dimensions $5 \times 5 \times 0.5$ mm. The GVMs in this crystal are large—$\mathrm{GVM}_{390}^{260} \approx 280$ fs/mm and $\mathrm{GVM}_{780}^{390} \approx 630$ fs/mm—and this negatively impacts the UV production efficiency. The blue pulse falls behind the red very quickly in this crystal, and since they will interact very little if the delay between them increases by only 30 fs, they only overlap and produce UV within the crystal for a distance of about $l_{\mathrm{eff}} = \frac{30\ \mathrm{fs}}{630\ \mathrm{fs/mm}} = 50\mu\mathrm{m}$. One fortunate effect of this self-limited interaction length is that it limits the UV pulse length. One can imagine that the $\mathrm{BBO_{SFG}}$ crystal is effectively only 50μm long, and thus the smear $\mathrm{Sm}_{390}^{260} = 14$ fs is short. We estimate that the UV pulses created should be of similar length to the blue pulses after $\mathrm{BBO_{SFG}}$.

The $\mathrm{BBO_{SFG}}$ crystal is aligned similarly to the $\mathrm{BBO_{SHG}}$ crystal, but there is one important parameter that has a large effect on the UV generation efficiency. The chirp of the red laser pulse (see section 2.1.1) can be controlled by adjusting the laser amplifier, and maximum UV conversion efficiency was *not* achieved when the red pulses were transform limited. This is unexpected since transform limited red pulses would have the highest peak intensity. In fact, the efficiency increases several-fold for negative chirps, with maximum efficiency being achieved when the red pulses are lengthened to over 200 fs.[1]

[1]The GVD_{780} of $\mathrm{BBO_{SHG}}$ is not large enough to significantly alter the length of the

The reason for this dependance on red pulse chirp is not well understood, but possibly can be traced the GVM in BBO_{SHG} and the poor overlap between the blue and red pulses in BBO_{SFG}. One can imagine that as the red pulses are lengthened that the amount of overlap between the red and blue pulses entering BBO_{SFG} increases. It's possible that this increase in overlap can result in higher UV generation efficiency even though the peak intensities of both pulses should be lower than in the case of transform-limited red pulses.

The maximum amount of power in the UV achieved was ~ 8 mW, which was sufficient for our experiments (chapters 4 and 5). The efficiency decreased over a period of several months to about half this, which was probably due to damage on the BBO crystals, which is visible. More evidence that this decrease in efficiency was caused by localized damage is given by the fact that, after the damage was discovered, changing where the beams hit the crystals improved the efficiency. This damage should be avoidable by not downcollimating the red beam.

3.2 Bichromatic prism pair interferometer

The bichromatic prism pair interferometer (BPPI) comes after the nonlinear frequency conversion setup and performs several functions. It removes the red pulses from the multi-color beam, allows control of the delay between the blue and UV pulses that remain, and allows independent control over the GVD (see section 2.1.1) experienced by the blue and UV beams. Because of

red pulses, so this is not a case of precompensation for BBO_{SHG} resulting in short red pulses downstream of it.

its general usefulness and degree of novelty, a relatively extensive treatment of the BPPI, including information and advice generally useful for someone potentially interested in using one will be given. Specific information about our device will follow.

The device traditionally used for the delay control mentioned above is a Mach-Zehnder interferometer, which uses dichroic beam splitters to separate and recombine the bichromatic beam in a wavelength selective fashion. A major problem with these devices is that the dichroic beam splitters are generally expensive, are only available for certain wavelength ranges, and often introduce dispersion that is unfavorable for ultrashort pulse work. If it is desired to use pulses of more than two different wavelengths at once, then the complexity and size of the device and constraints on the beam splitters increase quickly. The BPPI is more flexible with respect to the particular wavelengths used, can be more easily expanded to operate with more than two wavelengths at a time, and can be adjusted to give zero GVD to each beam that passes through it. In fact, it intrinsically allows the GVD experienced by each beam passing through it to be adjusted independently and continuously from positive to negative values, making it attractive where fine dispersion control is desired, such as when pulses must be precompensated for varying amounts of dispersive material in order to arrive at an interaction region in a near-transform-limited state.

3.2.1 General description

As we learned in section 2.1.2, prism pair compressors (PPC) have a continuously variable GVD including positive and negative values, and this is an important value to control for the propagation of ultrafast pulses. We also know that prisms can be used to separate multiply colored pulses in a beam through dispersion, so it makes sense to try to use prisms for GVD control and bichromatic interferometry at once. The BPPI does just this. The layout of the BPPI is shown in Fig. 3.3. The incoming collinear two-color beam is spatially separated by wavelength by refracting through the first, common prism in the interferometer (p_c). Then the separate beams, angularly dispersed themselves, pass through individual prisms (p_1 and p_2), retroreflect off of mirrors, and then pass through $p_{1,2}$ and p_c again. All prisms are matched and aligned such that the angular dispersion induced by the p_c is exactly undone, and the beams after one pass through the prism pair are collimated, although they are spatially chirped (Fig. 3.4). Placing one of the retroreflection mirrors on a delay stage allows control of the delay between differently colored pulses. A small vertical offset given to the beams by the retroreflection mirrors allows them to be separated from the input beam after they exit the interferometer.

As stated before, a particular advantage of the BPPI is that the arrangement can conceivably be used fairly easily with three or more wavelength beams at the same time, making it a multi-chromatic prism pair interferometer. One needs simply to add an additional prism and retroreflection mirror for each additional wavelength. Furthermore, this device could be useful for

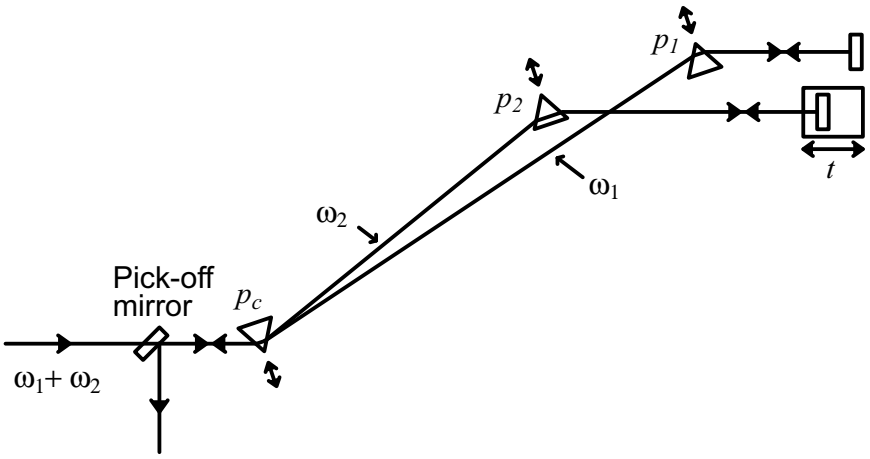

Figure 3.3: Layout of BPPI, consisting of only 3 prisms and three mirrors. The pick-off mirror has a small vertical offset. The incident and exit beams contains pulses of two central frequencies.

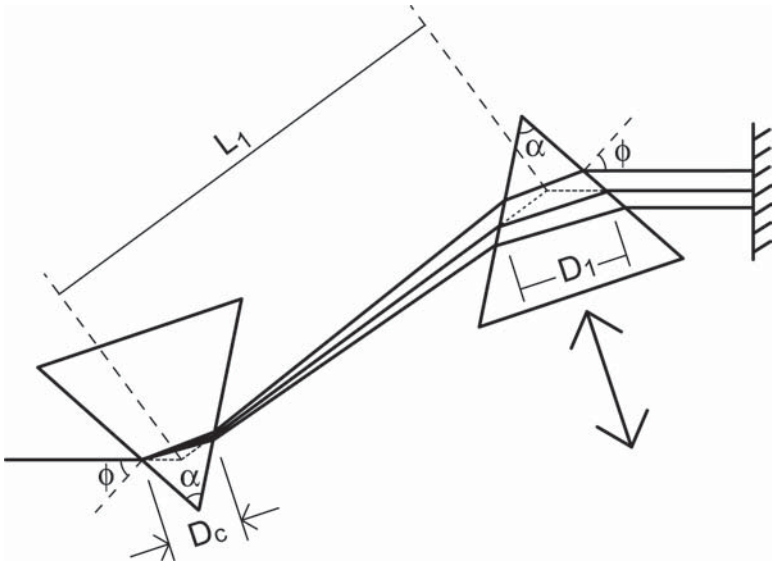

Figure 3.4: Layout of prism pair compressor, including definition of prism pair parameters, shown on one prism pair with rays representing the central, highest, and lowest frequency components of a single colored beam. The subscript c refers to the common, first prism, while numeric subscripts correspond to each individual prism in turn. Values of D are changed by adjusting prism insertion along direction shown by arrows.

beams that have large, continuous spectra, because it allows one to control which colors are transmitted by the device by using masks and slits, and to control the GVD and delay experienced by different parts of the spectra independently by using as many prisms as one wants. We have not experimented with such arrangements, and thus concentrate on the bichromatic case for this thesis.

One disadvantages of the BPPI is the high energy losses that it can cause due to surface reflections off of its many prism faces. This can be mitigated for at least the light at one central frequency by using prisms with anti-reflection coatings, or through selecting incidence to occur at Brewster's angle (if there is a beam that is p-polarized). Another disadvantage that should be mentioned is that if simple mirrors are used for retroreflection, then they can't *perfectly* retroreflect the beams because then separation between the input and output beams outside of the BPPI wouldn't be possible. The small angle placed on the beams because of this causes there to be a very small coupling between the motion of the delay stage and the vertical position of the beam that reflects from it. In situations where this is problematic, right-angle reflectors instead of the simple retroreflection mirrors can be used to lower the beam without changing its angle.

3.2.2 General design considerations

To design a BPPI for a specific situation, it is necessary to calculate the amount of dispersion expected from a certain prism configuration (see Fig. 3.4 for parameter definitions used below). The GVD of a PPC can be thought

of as the sum of its negative GVD, which is a function of its L, α, and ϕ values, and its positive GVD caused by travel through the prism material, which is a function of the values of D for the prisms. Analytical expressions exist [2, 23] for at least the second and third order dispersions of a PPC as a function of L, D, α, ϕ, and the dispersion characteristics of the prism material. However, we have found a computer model of a PPC that includes all of these parameters and is more useful. This model, present in an suite of LabVIEW programs designed for ultrafast laser physics modeling [17], allows one to easily simulate a beamline with a PPC and some (if needed) dispersive material present. Then one can determine which PPC parameters give the shortest possible pulse where one is needed. With these parameters, all GVD in the system should be precisely balanced, and one can see the effect of residual third order dispersion on the pulse.

When designing a BPPI, one must first decide on the prism material and apex angle to be used. The prism material of course needs to be transparent for all of the wavelengths used, and should usually have the largest value of first-order dispersion as possible in order to achieve maximum angular separation between differently colored beams and allow the highest possible negative GVD for a value of L constrained by table space[2]. The apex angle is important because there is a unique apex angle that satisfies two important conditions which help to improve BPPI performance and ease of use. The first condition is that it is customary for prisms in prism pair compressors to be

[2]If one is using very short ($<$ 30 fs) pulses and thus is concerned with third order dispersion, then minimizing this while maintaining acceptable first order dispersion should be a priority.

used at the angle of minimum deviation, which greatly simplifies alignment (see section 3.2.3). The second involves the angle of incidence, which is important because of its effect on reflective energy losses in the system. Since each beam passes through 8 prism-air interfaces during a trip through the BPPI, it's best to choose incidence angles on the prisms that minimize this loss. Brewster's angle (unfortunately possible only for a beam of one central wavelength) is of course a good choice for this if there is a p-polarized beam. For Brewster's angle for one wavelength $\theta_B^{\lambda_0}$ to be the same as the angle of incidence for minimum deviation, α must be equal to

$$\alpha = \arccos\left[(n_1/n_2)\sin\theta_B^{\lambda_0}\right] \quad . \tag{3.3}$$

Fortunately for some, there are stock prisms available that are cut to have apex angles that satisfy this for certain common ultrafast wavelengths like 800 nm.

Second, one must select the values L_1 and L_2 carefully in order to select an appropriate range of possible GVDs that can be reached, and to allow adequate clearance between the beams dispersed by p_c for insertion of the closer of p_1 and p_2. Once the prisms and retroreflection mirrors are in place, it is simple to adjust the GVD experienced by each beam by translating the prisms parallel to their apex bisectors (Fig. 3.4), thus changing the individual values of D. However, this movement is limited because of the proximity of beams of different wavelengths to each other.

When thinking about different prism arrangements for two beams, it can be seen that there are two different classes of arrangements of prisms, and

that there is an important difference between these classes concerning the coupling of the values of L and D for the prism p_1 or p_2 that is closer to the common prism. Defining the prism for the longer wavelength beam to be p_1, and the prism for the shorter wavelength beam to be p_2, then in the first arrangement class $L_1 < L_2$, and in the second $L_2 < L_1$ (Fig. 3.3 shows an arrangement of the second class). In general, as L is increased in a PPC, then the GVD will become more negative. Thus, for a given goal value for the GVD of a prism pair, as L is increased, D must also increase. For the first arrangement class, this coupling is problematic. If there is not enough clearance between beams for the insertion of p_1 at a certain value of L, then as one increases L to move towards where the beams are farther apart the simultaneously increasing value of D makes the clearance needed larger. Depending on the colors involved and the prism characteristics, it may be impossible to find an arrangement of the first class that works for some goal value of GVD. For the second class, in which it is p_2 that must clear the other beam, increasing L and D both increase the prism-beam spacing, making this arrangement class more likely to work in general.

3.2.3 Alignment procedure

The alignment of the BPPI is non-trivial, and is important for its performance. In order for each PPC to disperse and reconstruct its beam such that it has no remaining angular dispersion, the incident angle on p_c and exit angles on p_1 and p_2 must all be the same. Doing this requires rotating each prism about the y-axis (see Fig. 3.5), while having some way to determine

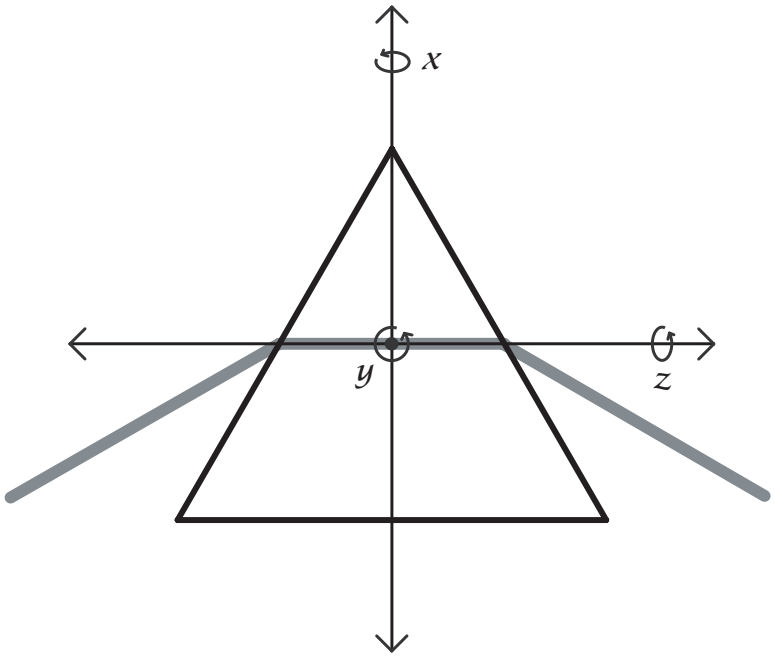

Figure 3.5: Definition of axes for adjustment and alignment of prisms. View is from above, and beam is shown at minimum deviation.

what angle to stop at. Also, care should be taken in setting the angle of the prisms around the z-axis as well. It's best if the prisms are mounted such that they can be rotated about these axes in a precise fashion, and such that rotation about the x-axis is set so that the base of the prism can be parallel to the optical table.

The alignment procedure that we used is as follows. First, the beam entering the BPPI should be level and travel with a well defined direction, *e.g.* along the holes in an optical table. Then p_c is inserted and rotated about the z-axis. If the z-axis angle is incorrect, then the prism will take a beam that is level with respect to the optical table and send it up or down, so the angle can be set by checking the output beams at large distances from the prism.

Next, p_c is rotated about the y-axis to set the incidence angle ϕ. There are two choices for ϕ that make this step particularly easy: the angle that corresponds to the angle of minimum deviation for the prism and Brewster's angle (of course, both of these are dependant on wavelength, so will be possible for only one wavelength component at a time). If Brewster's angle is used, then the first prism is simply rotated until minimum reflection from the surface is observed. If the angle of minimum deviation is used, then one rotates the prism while looking at the output beam at large distances. The proper position occurs where the beam is deflected the least. In either case, afterwards one knows ϕ precisely for p_c, and then must align p_1 and p_2 to have the same ϕ.

Prisms p_1 and p_2 are first placed in their respective beams at the proper positions for their values of L, and then they are adjusted about the z-axis like p_c was. They can then be adjusted for ϕ by noting that at the proper angle, their output beams will propagate down the table in the same direction as the original beam. If one is able to propagate the beams for a large distance to check the direction, then this method can be quite precise. However, if the angle of minimum deviation is used for one wavelength, then the second prism for that wavelength can be set in the same way as p_c, which is a somewhat easier procedure than trying to set a specific beam direction.[3]

Aligning the retroreflection mirrors of the BPPI is straightforward. First, one mirror is adjusted such that the beam returning from it coincides closely

[3]R.N. Coffee at the University of Connecticut has developed an alignment system for a BPPI that more precisely ensures the collinearity of the output beams, and doesn't rely on measuring any beam direction relative to the optical table. We have not yet experimented with this method.

with the input beam upstream of p_c, but with a small vertical offset necessary to hit a mirror. Then, the second retroreflection mirror can be adjusted to produce an overlap between the two beams at large distances after the BPPI.

3.2.4 Our BPPI device

Our BPPI uses fused silica prisms with apex angle $\alpha = 60°$, and 25 mm square faces. They are mounted on standard, two-axis adjustable, kinematic prism mounts, that allow rotation about the z- and y-axes. Unfortunately, it is not possible to mount the prism with this hardware such that the axes are located with respect to the prisms where they are in Fig. 3.5, which causes rotation to be coupled with prism translation as the mount is adjusted. This is not a problem for the z-axis adjustment or for y-axis adjustment if one is using Brewster's angle or checking the direction of the beam downstream of the prism against some reference, but it makes accurately finding the position corresponding to minimum deviation difficult, if not impossible. This is because, as one is looking at the beam downstream to find its minimum deflection, the motion observed is a combination of motion due to a change in the deflection angle and due to translation of the prism. The orientation of the prism that corresponds to minimum deviation will in general not be the same as the orientation that corresponds to a minimum in the position of the beam at some spot downstream. We may be subject to some small error caused this, which would result in a small angular dispersion in the reconstructed beams, but our biological experiments should not be sensitive to this and fixing this problem has not been a priority. In any case, for

those considering using a BPPI, the prisms *should* be mounted such that pure rotation about their center is possible.

Prisms need to be translated along the x-axis in order to change their D parameters, and this would be best accomplished by mounting the prisms on a translation stage. However, accuracy and repeatability at the 10 μm level is not necessary for this adjustment in most circumstances, so we used a more cost effective method to implement this movement. Our prism mounts are attached to rectangular bases, and the angle of these bases are set with respect to our optical table through two point contacts. If the direction of the translation isn't exactly along the x-axis, then as D is adjusted for a prism L will also be adjusted. This is a very small effect though, and will usually not be of concern.

Our prisms do not have an anti-reflection coatings, so there are significant power losses through the BPPI from Fresnel reflections. We know that our blue beam should be s-polarized because it should be perpendicular to our p-polarized red beam. For a typical incidence angle on the prism of 48.6° (which is the angle for minimum deviation of the UV beam), the Fresnel reflection of the blue beam is $R_{\|} = 0.10$. With all 8 prism-air interfaces present in one trip through the BPPI, and the retroreflection mirror which is aluminum and has a reflectivity $\approx 90\%$, the transmission efficiency of our BPPI for blue should be $T_{\mathrm{BPPI}} = 0.9^9 \approx 0.4$. The situation is much better for the UV because its polarization should be perpendicular to the blue, and 48.6° is not very far from Brewster's angle $\tan^{-1}(n_2/n_1) \approx 56°$. For the UV, $T_{\mathrm{bppi}} = 0.995^8 \cdot 0.9 \approx 0.86$.

3.3 Difference frequency cross correlation setup

In order to know the delay between the blue and UV pulses downstream of the BPPI, the point at which the pulses overlap there as a function of the position of the BPPI translation stage must be known. Once this "time-zero" point is found, the delay between the pulses can be set easily by measuring the position of the stage accurately. The speed of light is $c = 0.3\ \mu$m/fs, so femtosecond accuracy in setting the delay is possible if the stage can be positioned with precision at or below a micron. Finding time-zero requires the existence of a physical process that produces a signal only when both pulses are temporally overlapped. Sum frequency generation is just such a process, however, light at the sum frequency of 390 and 260 nm light has a wavelength of $(390^{-1} + 260^{-1})^{-1} = 156$ nm, which is deep in the ultraviolet and thus difficult to work with. So, instead we use difference frequency generation (DFG) to produce red light at 780 nm for this step.

The use of almost any method to determine when two pulses are overlapped allows a more information-rich measurement to be made—a cross-correlation of the two pulses involved. This measurement contains certain pieces of information about the lengths of the pulses that make it, and can be very informative if done in a certain way. We constructed an apparatus which allows us to measure spectrally resolved difference frequency cross-correlations (DFXC) of the blue and UV pulses, and describe it here.

3.3.1 Cross-correlations

To perform difference frequency cross-correlations, we send the collinear beam of UV and blue pulses leaving the BPPI into a BBO crystal ($\mathrm{BBO_{DFG}}$), and measure the energy of the red light pulses that are created as a function of UV-blue delay τ. The signal that we expect to see theoretically can be derived as follows.

In difference frequency generation with c.w. light and with perfect phase-matching and no pump depletion [3], the relationship between the two input field amplitudes (called the "pump" E_{P} and "signal" E_{S} fields, for the higher and lower frequency light, respectively) and the output field amplitude (called the "idler" field E_{I}) for a crystal of length l is [3]

$$E_{\mathrm{I}} = C_1 \frac{E_{\mathrm{P}}}{|E_{\mathrm{P}}|} E_{\mathrm{S}} \sinh C_2 |E_{\mathrm{P}}| l \,, \tag{3.4}$$

where C_1 and C_2 are constants. If

$$C_2 |E_{\mathrm{P}}| l \ll 1 \,, \tag{3.5}$$

then we can write for the field amplitudes

$$E_{\mathrm{I}} = C_3 \frac{E_{\mathrm{P}}}{|E_{\mathrm{P}}|} E_{\mathrm{S}} |E_{\mathrm{P}}| \,, \tag{3.6}$$

and intensities

$$I_{\mathrm{I}} \propto |E_{\mathrm{I}}|^2 = |C_3 E_{\mathrm{P}} E_{\mathrm{S}}|^2 \propto I_{\mathrm{P}} I_{\mathrm{S}} \,. \tag{3.7}$$

For pulses which have slowly varying field amplitude envelopes, we can re-

place I with $I(t)$, and from eq. 3.7 we can write

$$I_{\mathrm{I}}(t,\tau) \propto I_{\mathrm{P}}(t) I_{\mathrm{S}}(t-\tau)\ , \tag{3.8}$$

where τ is the delay between pump and signal pulses. The signal that we measure in the end (I'll call it XC(τ)), is the total power of the idler beam as a function of τ, and it can now be written as

$$\mathrm{XC}(\tau) \equiv P_{\mathrm{I}}(\tau) \propto \int_{-\infty}^{\infty} I_{\mathrm{I}}(t,\tau)\, dt = \int_{-\infty}^{\infty} I_{\mathrm{P}}(t) I_{\mathrm{S}}(t-\tau)\, dt\ . \tag{3.9}$$

This is recognizable as the mathematical definition of the convolution of I_{P} and I_{S}.

There are two notable potential problems with the above derivation. The first is that eq. 3.8 is only true if there is no smear (see eq. 3.2) present in $\mathrm{BBO_{DFG}}$. Our $\mathrm{BBO_{DFG}}$ is thin, but it does have a small smear, which has an effect which is described below. The second problem is that one needs to be sure that the relationship in eq. 3.5 is true. We estimate that we have operated at a point where this is uncomfortably close to being untrue, and state the possible consequences of this below as well.

If the relationship in eq. 3.9 hold true, then good information is immediately available about the lengths of the pump and signal (in our case, the UV and blue) pulses. If these pulses are roughly Gaussian in shape, then we know mathematically that the FWHM of the cross-correlation as a function of τ, written $\Delta\tau_{\mathrm{XC}}$, is related to the FWHM of the pulses Δt_{P} and Δt_{S} by

the simple relationship

$$\Delta\tau_{\mathrm{XC}}^2 = \Delta t_{\mathrm{P}}^2 + \Delta t_{\mathrm{S}}^2 \; . \tag{3.10}$$

If the pulses differ significantly from a Gaussian form, then eq. 3.10 will fail, but in any case one can at the very least state that $\Delta t_{\mathrm{P}} < \Delta\tau_{\mathrm{XC}}$ and $\Delta t_{\mathrm{S}} < \Delta\tau_{\mathrm{XC}}$, so one can place an upper bound on the lengths of the pulses involved.

If there is a significant amount of smear in the crystal used to do DFG, then it will result in an increased value of $\Delta\tau_{\mathrm{XC}}$. One can easily see that this is true by imagining a crystal that is very thick and has a large $\mathrm{GVM}_{\mathrm{S}}^{\mathrm{P}}$ value. If the pump and signal pulses don't overlap temporally outside of the crystal, then it's still possible to create an idler pulse if the higher frequency and thus slower moving pump pulse leads the signal at the crystal entrance, but the signal pulse overtakes it within the crystal. If the smear is of comparable length to the pump and signal pulses, then the following relationship is true :

$$\Delta\tau_{\mathrm{XC}}^2 = \Delta t_{\mathrm{P}}^2 + \Delta t_{\mathrm{S}}^2 + (\mathrm{Sm}_{\mathrm{S}}^{\mathrm{P}})^2 \; . \tag{3.11}$$

If the idler pulse in a DFXC is sent into a spectrometer, then a spectrally resolved DFXC can be taken. This pulse measurement technique is exactly equivalent to a technique known as difference frequency generation cross-correlation frequency-resolved optical gating (DFG XFROG) [24]. This technique combines this measured set of spectra as a function of τ with an algorithm that allows one to fully determine the electric field as a function of time of one of the input pulses **if** the $E(t)$ of the other pulse is already

known. This is not the case for us, but the spectral information is still useful because it can indicate whether one or both pulses has a spectral chirp. If either of them does, then the resulting DFXC trace will show a chirp as well.

3.3.2 Our DFXC setup

Our DFXC setup is not complex (Fig. 3.1)—it contains only 3 main components. The first is a BBO crystal cut with $\theta = 57.2°$ and having dimensions $5 \times 5 \times 0.1$ mm. We wanted this crystal to be particularly short because of the smear effect mentioned above. For this crystal $\mathrm{Sm}_{390}^{260} = 28$ fs, which is significant, but not so much that it dominates the value of $\Delta\tau_{\mathrm{XC}}$. The next component is a Schott RG610 absorptive long-pass filter which passes the newly created red idler beam while blocking the UV and blue light. Next comes the spectrometer, which is an Ocean Optics USB2000 that we focus into and read with a computer.

DFXC data is taken with a computer running a custom made LabVIEW program that interfaces with the delay stage and spectrometer. The delay stage is fitted with a Zaber T-HLA heavy-duty stepper-motor actuator that is operated in open-loop mode, with no distance encoder present. This actuator has a resolution of 0.1μm and a stated repeatability of $< 0.4\mu$m, which correspond to 0.33 and < 1.3 fs, respectively. These values are more than small enough to resolve the pulses that we create, which have minimum lengths of tens of femtoseconds. The LabVIEW program sends a signal to the stage to move, reads the spectrometer, and repeats across the entire range of the DFXC. An example of three spectrally resolved DFXC traces

are shown in Fig. 4.1.

The DFXC idler beam power was very noisy and an averaging procedure was used to improve the data. The largest source of this noise is most likely the noise present in the energy of the red pulses coming from the laser system. This noise itself is relatively small (around 5% typically), but it is amplified by the non-linear nature of the sum and difference frequency generation. The energy of the blue pulses created in the BBO_{SHG} crystal depends on the square of the red pulse energy. The UV pulse energy then depends linearly both on the blue and red pulse energies, so it is proportional to the third power of the red pulse energy. Then the UV and blue pulses mix to make red pulses that have a power that depends linearly on each of them, and thus is proportional to the fifth power of the original red pulse energy .

If this noise consisted of fluctuations that occurred only on short time scales (*e.g.* less than one second), then a single scan of the delay could be completed while averaging each DFXC spectrum generated for several seconds. However, there are significant fluctuations in DFXC signal that occur on timescales as long as tens of seconds and even minutes. These drifts are likely due to thermal fluctuations in the pump laser and the amplifier. Instead of taking one scan while averaging each data point over very long time scales, we instead took several "fast scans" and averaged them together afterwards. This way, the pulses that were averaged together to make each data point in the final trace were spread more evenly throughout the time taken to record the trace, and power fluctuations that occurred over time scales that were long compared with this time were less likely to result in

artificial fluctuations or drifts present in the trace.

3.3.3 Alignment, finding temporal overlap, and optimization for data taking

Alignment into BBO_{DFG} proceeded as follows. The beam was not focused, and an iris was used to restrict the beam size to an area smaller than that of the 5×5 mm face of the crystal. Finding the initial overlap of the pulses was difficult, because there are many parameters that must be simultaneously correct to see the signal. The proper orientation of BBO_{DFG} to achieve phasematching was determined by replacing the thicker BBO_{SFG} crystal with it in the NLF setup. Since the two crystals are both cut to nearly the same angle θ,[4] the thinner crystal can also be used to create UV, and the orientation at which this is most efficient is the same as the orientation required to produce red light most efficiently with DFG.

Once the orientation of the crystal is close to being optimal, the next challenge is to place a detector at the right position to see the red pulses when they are created. The simplest, general way to do this is to remove the long-pass filter and align the detector to receive the blue and UV beams. It is easiest if the detector has a large surface area for this, and for this reason a photodiode was used to find temporal overlap at first before using a spectrometer which has a very narrow entrance slit. One other detector align-

[4]They should be cut to *exactly* the same angle because the phasematching conditions for both are exactly the same. The difference in θ between the two is accidental. Note that the angle θ that beams see when passing through a crystal can be adjusted slightly by rotating it about the proper axis, so good phasematching is possible although θ might be slightly off.

ment method that was used relied on red light that reflected diffusely from the beam block in the red arm of the BPPI (Fig. 3.1). This light returned through p_c and traveled with the UV and blue beams through BBO_{DFG} and the long-pass filter to the detector. The detector could be moved to see this light, and then was close to the optimal position to see the red DFXC light. Luckily, the DFXC pulses were delayed relative to the diffuse reflection pulses and were much more powerful than them, so the diffuse light didn't interfere with the DFXC detection.

To achieve temporal overlap, the delay stage of course has to be positioned such that the path lengths of the two arms of the BPPI are the same. So, the lengths of the two arms of the BPPI were measured with a tape measure to an accuracy of a few millimeters in order to have a good initial guess for the stage position. When the above steps were taken, the DFXC signal could be found by translating the delay stage slowly by hand while looking at the photodiode signal on an oscilloscope.

Once the overlap was found, the delay stage was parked at the peak of the signal intensity, and several parameters were optimized to achieve maximum signal strength. The most important was UV-Blue spatial overlap, which was adjusted by moving the blue beam's retroreflection mirror. The second was the BBO_{DFG} orientation, which could then be set with reference to the actual red signal being produced. The final parameter was the alignment into the spectrometer, which was very sensitive to beam position.

Returning to the issue of possible non-linearities in the dependance of the DFXC idler beam on the pump beam intensity, we estimated the value of

$\xi \equiv C_2|E_{\mathrm{P}}|l$ to determine if eq. 3.5 was valid. We calculate that the average electric field strength of our UV pump pulses, which have around 3 μJ of energy and a spot size of ~ 1 mm when they reach the $\mathrm{BBO_{DFG}}$ crystal, is 3×10^8 V/m. The factor C_2 is equal to [24]

$$C_2 = \sqrt{\frac{16\pi^2 d_{\mathrm{eff}}^2}{n_{\mathrm{S}} n_{\mathrm{I}} \lambda_S \lambda_I}} \approx 10^{-5} \frac{1}{V} \,, \tag{3.12}$$

for our setup (d_{eff} is a crystal parameter that indicates the strength of the non-linear interaction), and $l = 0.1$ mm, so $\xi \approx 0.3$ on average for our UV pulses. Since $\sinh 0.3 = 0.305$, it can be said that $\sinh x \approx x$ for this value of ξ, but it is possible that ξ could have a peak value of a few times this depending on the exact temporal and spacial extent of our UV pulse. As ξ gets larger, the linear nature of the DFG breaks down, and the pump pulses that create the DFXC trace become effectively narrowed—their peak values are amplified and their FWHM values are thus reduced. Thus, if one uses the DFXC width $\Delta\tau_{\mathrm{XC}}$ to estimate Δt_{P}, the estimations will tend to be smaller than the actual pulse width. We do not expect that this is a large problem with our setup, but it would certainly be prudent to check this effect if it were desired to gain accurate qualitative data about the pump pulse length from the DFXC traces. One simple method for checking it would be to compare DFXC traces obtained while using our 3μJ UV pulses with those obtained while using attenuated UV pulses.

3.4 Self-diffraction setup

When working with the BPPI, it was often useful to find the prism positions that corresponded to the minimum pulse lengths for the UV and blue pulses. This is equivalent to finding the GVD values of the PPCs that cause the output pulses to have zero second order spectral phase. One way to do this is to move the prisms (usually prism insertion alone) in small increments, and take DFXC traces at each position. The DFXC trace width $\Delta\tau_{\mathrm{XC}}$ as a function GVD for one of the beams should go through a minima at the same point that Δt goes through a minima for that beam. One major problem with this technique is that it takes several minutes to perform a good DFXC trace with sufficient averaging, and thus taking several traces at different values of GVD to find a minima can take 15-30 minutes. In order to perform this task more quickly and accurately, we developed a system based on self-diffraction (SD), a third-order non-linear effect that operates on one beam at a time. With this system, the minimum pulse length (and thus minimum second order phase) for either color can be found quickly, because it produces a signal which varies in real time with the maximum pulse intensity and thus minimum pulse length.

One other motivation for building this device is that we noticed some odd results in the initial data taken with the DFXC. We saw that the position of p_1 that corresponded to a locally minimum value of $\Delta\tau_{\mathrm{XC}}$ could itself possibly depend on the position of p_2. This indicates that it's possible to set D_2 such that the minimum $\Delta\tau_{\mathrm{XC}}$ as a function of D_1 does not occur when Δt_1 is also at a minimum. It is not known how exactly this occurs, although we

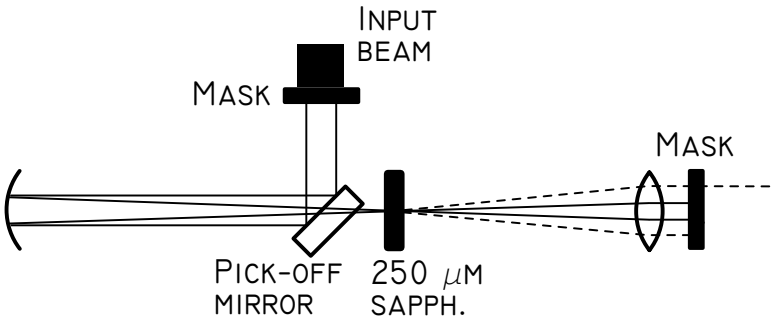

Figure 3.6: Layout of SD setup. Input beam goes through a double slit mask to form two thin beams. Output beam goes to spectrometer (not shown).

speculate that it's possible that cross-correlating oppositely chirped pulses could result in artificially short values of $\Delta\tau_{\mathrm{XC}}$. If the blue and UV pulses are oppositely chirped, *i.e.* one has negative and the other positive chirp, then at relatively large delays between the two the lowest (or highest) frequency components of *both* pulses will be the only frequency components that interact. Since in all phasematching processes there is a limited bandwidth at which good phasematching and thus good conversion efficiency occurs, these hi-hi and low-low frequency tail interactions would be expected to produce a weaker DFG idler pulse than one would expect from the instantaneous intensities in these tails alone. This source of pulse-frequency-based confusion can be eliminated by first minimizing the chirp for both pulses before taking difference frequency cross correlations. When this is done, we know that the instantaneous frequency across the pulse is close to being constant, and we can thus ignore frequency dependencies in the DFG conversion efficiency and concentrate on instantaneous intensities alone, like in eq. 3.7 and the derivation that follows it.

The layout of our SD setup is shown in Fig. 3.6. The input beam goes

through a double-slit mask (the slits are not narrow enough such that significant diffraction occurs) so that two beams are created. These beams are directed by a flat mirror onto a $f = 10$ cm curved mirror, with incidence as normal as possible. The curved mirror focuses the beams and crosses them, and at this point a 250μm thick sapphire window (which is used because sapphire has a high non-linear polarizability) is placed. Inside the sapphire, the two beams interfere with each other to create a fringe pattern of regions of alternating high and low electric field intensity.

We know in nonlinear optics that high optical field strengths inside of a material can locally change the index of refraction of that material through what is called the optical Kerr effect [3]. Thus the interference fringes in the sapphire produce an oscillating index of refraction, which acts as a grating that diffracts portions of the two incoming beams in the directions shown in Fig. 3.6. One of these diffracted beams passes through an output mask, and can be sent into a spectrometer or photodiode to measure its spectrum and power.

This pulse measurement setup is equivalent to a pulse characterization technique called self-diffraction frequency-resolved optical gating (SD FROG) [21], except for one difference. In SD FROG, the incoming beam is split with a beam splitter, and one of the resulting beams is delayed relative to the other before entering the crystal. Spectra of the diffracted beam are taken as the delay is stepped, and the resulting trace can be used to fully characterize the $E(t)$ of the pulses through the use of an iterative phase-retrieval algorithm. (This is similar to the DFG XFROG technique mentioned in sec. 3.3.1.) Since

the delay between the pulses in our two beams is always zero, we are not able to use this setup to do this characterization[5]. However, we can use the SD FROG theoretical background to analyze our SD setup.

We know that for an SD FROG setup, the electric field of the signal pulse (in this case, the diffracted beam) is given by [21]

$$E_{\text{sig}}(t,\tau) = E(t)^2 E^*(t-\tau) \ , \tag{3.13}$$

where $E(t)$ is the electric field of the input pulse and τ is the delay between the two pulses that were split from the same beam. Since $\tau = 0$ always in our SD setup, we can write

$$E_{\text{sig}}(t) = E(t)|E(t)|^2 \tag{3.14}$$

and further

$$I_{\text{sig}}(t) \propto |E_{\text{sig}}(t)|^2 = |E(t)|^6 \propto I(t)^3 \ . \tag{3.15}$$

Integrating with respect to time gives us

$$\mathcal{E}_{\text{sig}} \propto \int_{-\infty}^{\infty} I_{\text{sig}}(t)\, dt \propto \int_{-\infty}^{\infty} I(t)^3\, dt \ , \tag{3.16}$$

where $\mathcal{E}_{\text{sig}}$ is the total energy in the signal pulse, which is proportional to the signal that is actually measured, a power. In other words, the power of the diffracted beam is proportional to the time-integral of the intensity of the

[5]We have considered modifying our setup to create a SD FROG or similar "transient grating FROG" (TG FROG) setup [21, 9], and this is a promising direction for future work.

pulses in the input beam raised to the third power. Since the total energy in each input pulse is conserved and the shape of these pulses can't be very complex, the way to maximize this integral is to make the peak as intense as possible and thus the pulse as short as possible.

Aligning the SD setup is only slightly more difficult than aligning the DFXC setup. The only significant step is the adjustment of the mask that creates the two beams from the input beam. If too much power is transmitted in the two beams, then diffracted beams at higher orders than the first order beams shown in Fig. 3.6 will be created. These beams are undesirable because they complicate the SD measurement theoretically and practically, so it is best to attenuate the input beams until these higher order beams are not seen. If it is not possible to restrict the input energy enough through making the slits narrow because of diffraction effects, then the input beams can be masked in the perpendicular direction, forming points eventually rather than slits.

Like the pulses created in the DFXC setup (see section 3.3.2), the pulses in the SD diffracted beam have a large power noise. However, since the SD process is a third-order non-linear process, the SD signal pulse powers have sixth (when used with the blue beam) and ninth (when used with UV) order dependencies on the red pulse power, and are thus even noisier than the DFXC pulses. I attempted to measure the relationship between power in these pulses and D_1 or D_2 by using a spectrometer and averaging many thousands of pulses, but found that the position of the maximum could be found by eye much more quickly and with only slightly less accuracy than

through this method.

Chapter 4

Characterization and Proof-Of-Concept Experiments

To test the basic functionality of the devices built, several quick tests of expected performance characteristics and relationships between parameters were performed. With a couple of notable exceptions[1], the devices performed reasonably close to expectations, and no observed characteristics threatened the ability of the device to perform the functions required by its primary purpose—those defined by the crosslinking experiment detailed in Chapter 5. For this reason, details of every small test will not be given, and instead one experiment which encompasses the functioning of every subsystem of the experimental apparatus and successfully demonstrates its suitability for the delay and GVD control of a bichromatic collinear beam of blue and UV pulses will be presented. Also, preliminary results of another experiment will be reported which point towards the broader usefulness of the bichromatic prism pair interferometer for the manipulation and characterization of light

[1]See discussions about the UV conversion efficiency dependance on red pulse chirp in section 3.1.2 and about the DFXC with chirped pulse problems in section 3.4

that falls anywhere within the visible, near-IR, and near-UV portions of the spectrum and within two orders of magnitude of pulse duration.

4.1 Precompensation experiment

The goal of the first experiment that will be reported is to demonstrate two things: first, that the GVD that a beam experiences while passing through a BPPI is consistent with what we can easily calculate for a similarly arranged PPC, and second, that the BPPI can successfully precompensate both blue and UV pulses for a relatively large amount of dispersive material, accomplished by only adjusting the insertion of the prisms of the device. Once again (see section 2.1.1), precompensation in this context means the introduction of negative group velocity dispersion (GVD) to the beams to balance out positive GVD present in almost all optically transparent materials, and "successful" precompensation means that after the insertion of the material lengthens the pulses in both beams, their shapes and widths can be restored to nearly their original condition.

4.1.1 Procedure and data

To perform the precompensation experiment, the first task was to determine what BPPI arrangement was best suited for the required goals, and to calculate the exact BPPI parameters for zero GVD in this arrangement. The original goal was to be able to place the largest amount of dispersive material in the beam downstream of the BPPI as possible, while still being

able to precompensate the pulses for it though changing the prism insertions alone. This required that the setup have large values of L to provide the largest possible values of negative GVD when the values of D were small. An arrangement where L_1 (which corresponds to the blue beam) was larger than L_2 was selected, and the parameters that were necessary for the satisfaction of the above requirements while being expected to correspond to zero GVD for both beams were calculated.

Table 4.1: Different sets of BPPI parameters used for experiments.

	λ_1 nm	λ_2 nm	α $^\circ$	θ $^\circ$	L_1 cm	L_2 cm	D_c mm	D_1 mm	D_2 mm
OPT	390	260	60	48.6	124.5	56.5	18.9	18.1	21.5
CALC			(Same)					19.2	24.2
MAT			(Same)				11.4	11.7	15.4
Δ							-7.5	-6.4	-6.1
ORANGE	780	589	60	46.6	96	133	10	5	12

OPT–optimized for maximum SD signal, no material present. CALC–expected to correspond to zero GVD. MAT–optimized for maximum SD signal, with dispersive material present. Δ–difference between optimized positions before and after material insertion. ORANGE–parameters used for orange-light experiment detailed in sec. 4.2.

Next, the BPPI was set and aligned to the design parameters, and $D_{1,2}$ were adjusted to actually produce blue and UV pulses of minimum width, as determined through use of the SD setup. The SD signal was maximized by eye. The BPPI parameters of the optimized setup are shown in the first row of Tab. 4.1. These experimentally determined parameters are not far from parameters calculated to correspond to zero GVD for both beams, which are shown in the second row of the same table. The differences between

the two sets of values are small, and could certainly arise from many small errors in position measurement in the setup. One other likely explanation for the discrepancy is that it would be expected that the UV and/or blue pulses arrive at the BPPI already having some non-zero second-order spectral phase, especially since the red pulses from the laser system were themselves not optimized to have zero second-order spectral phase when this experiment was done. In any case, the PPC simulations provided a very good starting guess for the proper parameters.

Once the BPPI was optimized to produce blue and UV pulses of minimum length, a DFXC trace was taken. This trace is displayed in the first panel of Fig. 4.1, and is an average of 8 scans taken in succession (see discussion of "fast scans" in sec. 3.3.2). During each scan, the spectrum that was recorded for each delay was an average of 6 spectra taken in succession, and each of these spectra were obtained by collecting light on the spectrometer's CCD for 20 ms. Therefore, there were $20 \times 6 \times 8 = 960$ laser pulses averaged for each spectra seen.

The FWHM of this first trace is $\Delta\tau_{\mathrm{XC}} = 63 \pm 2$ fs. This will be referred to as $\Delta\tau_{\mathrm{XC}}^{\mathrm{opt}}$. This, and all following DFXC trace widths were determined through fitting a Gaussian function to the integrated signal. Gaussian functional forms were used because of convenience and because they were a good choice for most DFXC traces seen. In this specific case, it is true that the shape of the integrated trace departs from the Gaussian form. However, pulse width is generally far more important than specific pulse shape for the purposes of this entire project (see Chapter 5) and so there is justification

for approximating the pulses and their DFXC traces as Gaussians. The 2 fs error reported reflects the variability of $\Delta\tau_{\mathrm{XC}}$ seen between successively recorded traces.

After the DFXC trace of the optimized pulses was measured, dispersive material was placed into the beam after the BPPI. Specifically, a fused silica cuvette (which was designed for use with spectrophotometers and has a 1 cm internal path length and 1 mm thick walls) filled with water and a 1 cm cube of crystalline potassium dihydrogen phosphate (KH_2PO_4, called KDP for short), were used. KDP is a birefringent crystal like BBO that is used frequently for non-linear frequency conversion. The total amount of GVD expected for a beam passing through this material is shown in Tab. 4.2.

Table 4.2: Accounting of total GVD [fs^2] expected for material placed in beam.

λ/Material	2 mm Fused Silica	1 cm water	1 cm KDP	Total GVD
260 nm	420	2680	1740	4840
390 nm	200	970	1460	2630

KDP is birefringent, and the values for this material take into account the polarization of the beams and the orientation of the crystal. GVD values for water were obtained using [16].

To gauge the effect of the dispersive material on the pulses, a second DFXC trace was taken with the material present, but otherwise in the same way that the first DFXC data was taken. This trace is shown in the second panel of Fig. 4.1. The value of $\Delta\tau_{\mathrm{XC}}$ for this trace ($\Delta\tau_{\mathrm{XC}}^{\mathrm{mat}}$) is 207 ± 2 fs. This is a significant increase over$\Delta\tau_{\mathrm{XC}}^{\mathrm{opt}}$, but unfortunately is not what one would expect if one assumes that the original length of both pulses should be less

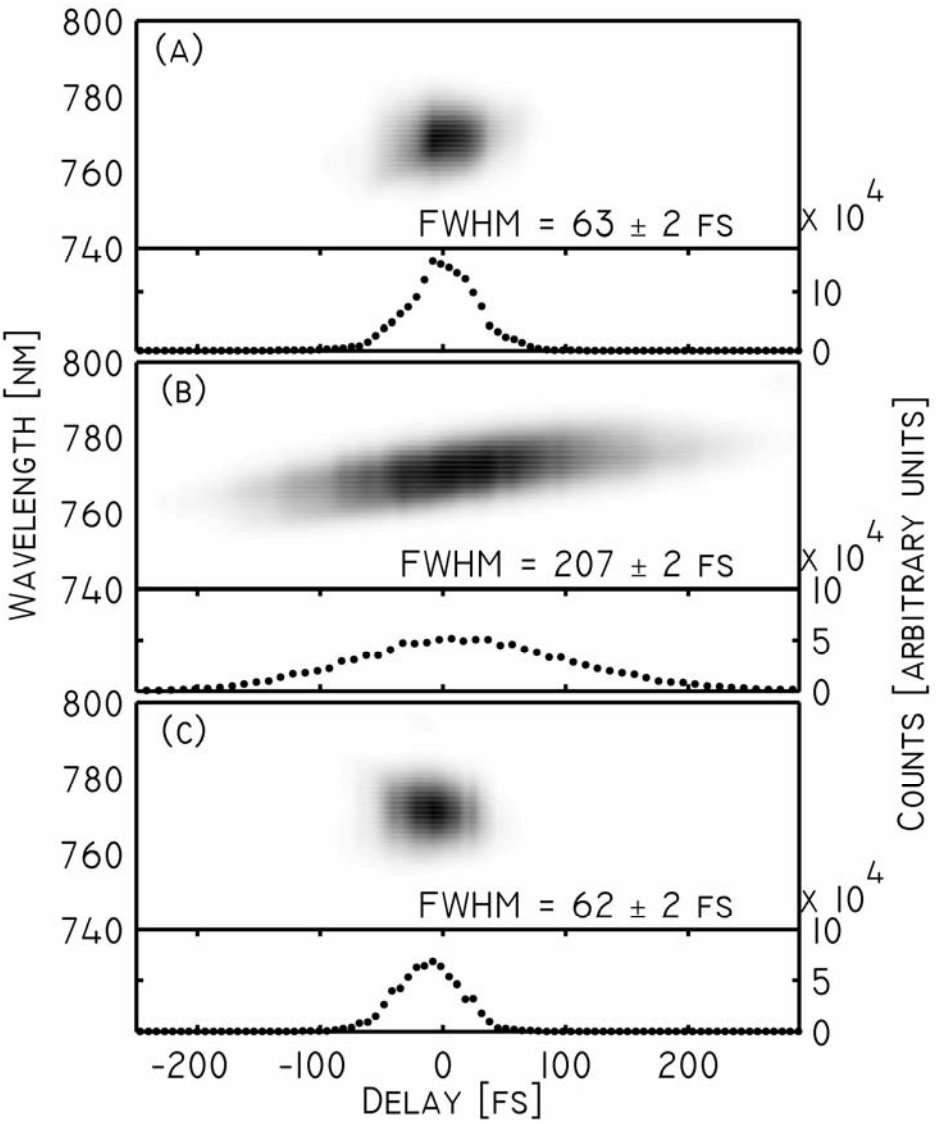

Figure 4.1: DFXC traces taken for precompensation experiment. The cross correlations were spectrally resolved, and darker colors correspond to higher intensities. The signal integrated over all wavelengths is displayed beneath each trace. Widths were determined by fitting Gaussians to the integrated signal. (a)–SD signal optimized for no material and no material is present. (b)–SD signal optimized for no material and material *is* present. (c)–SD signal optimized for material and material is present.

than $\Delta\tau_{\mathrm{XC}}^{\mathrm{opt}}$. This discrepancy will be discussed in the next section.

The final steps of this experiment were to re-maximize the SD signal for both of the beams with the material present, and then take a final DFXC trace to see if the original pulse widths were restored. The SD signal again was optimized by eye for each color individually while moving the prisms (the insertion of all three prisms were adjusted), and the new optimal values for the BPPI parameters are shown in row three of Tab. 4.1. The fourth row of the table shows the amount of prism material that was removed at each prism, and these values can be used to calculate the total amount of positive GVD that was *removed* from each beamline, to see if this is equivalent to the amount of GVD that was added with the water, fused silica, and KDP. The final DFXC trace was taken in the same way as the first two, and is shown in the final panel of Fig. 4.1. It's width is $\Delta\tau_{\mathrm{XC}}^{\mathrm{matopt}} = 62 \pm 2$ fs.

4.1.2 Precompensation experiment conclusions

The amount of fused silica that was removed through changing values of D to re-maximize the SD signal after the dispersive material was added is close to what was expected. For the blue beam, the change in the amount of fused silica traveled through in one trip through the BPPI was $\Delta D_{\mathrm{tot,b}} \equiv 2(\Delta D_c + \Delta D_1) = -27.8$ mm, with the factor of 2 being present because the beam travels through each prism twice. The GVD that corresponds to this thickness of fused silica is 2820 fs^2, which is different from the GVD that the dispersive material was expected to add (2630 fs^2) by 7%. Similar calculations for the UV beam give a value of 5640 fs^2 for the removed GVD,

which is 17% different from the expected addition of 4840 fs^2. Several sources of error might have contributed to this discrepancy. Most importantly is the inaccuracy of finding the maximum SD signal by eye, which is difficult because the signal is very noisy and does not change rapidly at its maximum as a function of D. A standard uncertainty in the proper value of D of 1 mm is not unreasonable for this process, which corresponds to an uncertainty in the proper value of ΔD_{tot} for each beam of $\approx 15\%$. With this in mind, it is not unreasonable to say that this data is consistent with the claim that the GVD experienced by a beam in our BPPI is the same as that experienced by an identical beam in a PPC having the same parameters, and that this GVD can be changed by changing values of D in a way that is expected.

These conclusions make no reference to the DFXC data from the experiment, and these data are somewhat problematic. Unfortunately, as was stated in section 4.1.1, the width of the DFXC trace taken after inserting the dispersive material and before precompensating for this insertion, $\Delta\tau_{\text{XC}}^{\text{mat}}$, is not as long as one would expect from the value of $\Delta\tau_{\text{XC}}^{\text{opt}}$. [Note to MSI committee members: this issue has not quite been resolved, and we are expecting to present a resolution to it at the thesis defence.]

Regarding the values of $\Delta\tau_{\text{XC}}^{\text{opt}}$ and $\Delta\tau_{\text{XC}}^{\text{matopt}}$, it is easily seen that they are nearly equal. This supports well the claim that the BPPI has the ability to successfully precompensated blue and UV pulses such that their pulse widths can be recovered after the insertion of large amounts of dispersive material.

4.2 Cross-correlation experiment with long, 589 nm pulses

Preliminary results of one other newly started experiment that uses the BPPI will be reported here. The purpose of this experiment is to characterize in some way interesting light pulses that are created in a different experiment in our laboratory through cross-correlating them with collinearly propagating red pulses that were used to create them.

The light pulses in question are orange 589 nm pulses made by the excitation of sodium vapor by *shaped* laser pulses from our laser system with a central wavelength of 780 nm and an energy of 100 μJ. By properly shaping these red pulses (using a pulse shaper connected to a genetic algorithm [8] which feeds back on the orange light signal) and focusing them into sodium vapor contained within a heat pipe oven, an intense coherent beam of orange light pulses is emitted that propagates in the direction of the red pulses [19, 20]. Characterization of these orange pulses is an important aspect of understanding the physics underlying their generation.

To perform a cross correlation of these copropagating orange and red pulses, the BPPI was rearranged to accommodate these two wavelengths with minimum GVD. The BPPI parameters used are shown in Tab. 4.1. Instead of using DFG to create light for cross-correlating the two pulses, sum frequency generation in BBO was used to create UV light at 336 nm. We successfully performed several sum frequency cross-correlations (SFXC) of the two pulses with the BPPI, and one SFXC trace is shown in Fig. 4.2.

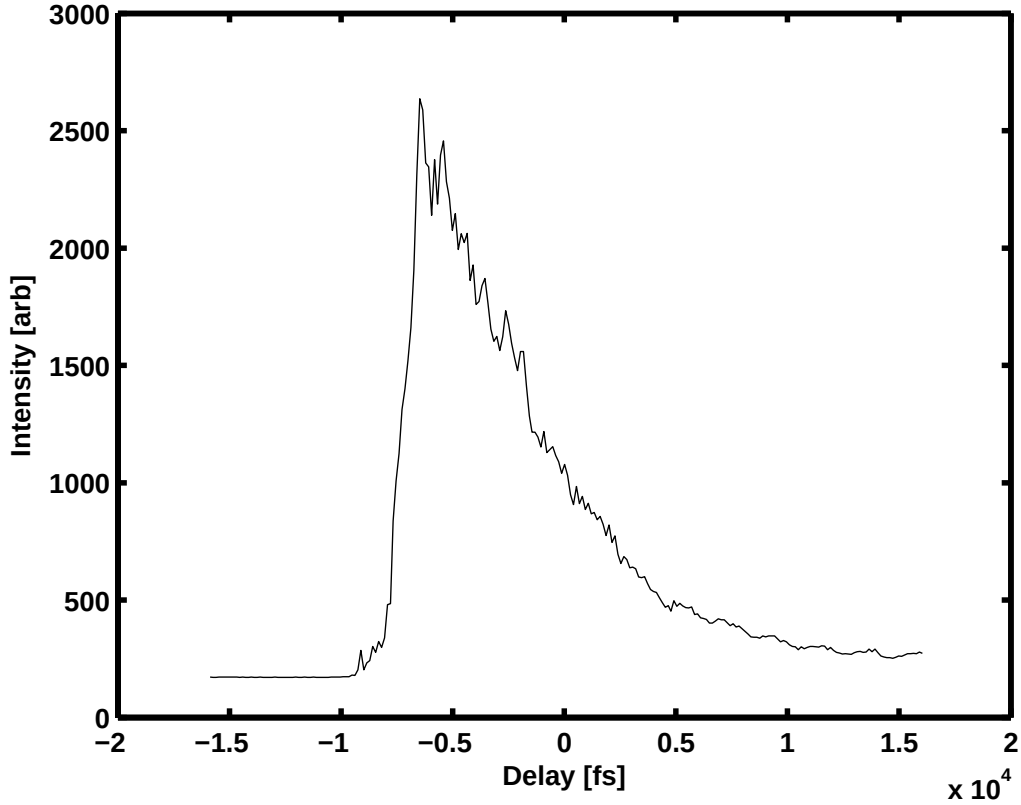

Figure 4.2: Sum frequency intensity cross-correlation of orange and red pulses. FWHM of trace is ~ 6 ps.

We know from separate measurements that the spectral bandwidth of the orange pulses is less than 1 nm, and thus they will be longer than 500 fs.

This experiment demonstrates well the flexibility of the BPPI. A simple rearrangement of components allowed the BPPI to be used with light at two entirely different wavelengths and intensities than we had originally planned its operation for, and we were able to do cross-correlations of the two pulses after buying only a suitable non-linear crystal and a filter for separating the UV SFXC signal after its creation.

This thesis has concentrated on the usefulness of the BPPI as a device for the manipulation of beams that are thereafter used for some experiment, not as a device useful for pulse characterization. However, the BPPI with SFXC setup can be used to characterize the orange light pulses with some useful level of accuracy for a few reasons. First, we already know quite a bit about the red pulses that we are cross correlating with the orange, and second, small errors in guessing the red pulse length and shape are made less important because of the large difference between the lengths/bandwidths of the red and orange pulses. Furthermore, there is little reason to be concerned with small errors in setting the BPPI to have zero GVD for the orange beam, which would distort it before its SFXC characterization, because the narrow orange light bandwidth makes it unsensitive to the small GVDs we would expect to be present. In fact, if this small GVD problem is acceptable, and it's possible to fully characterize the red pulses after propagation through the BPPI using the pulse characterization system already set up in our lab (SHG FROG, see [11]), then it should be possible to fully and accurately characterize the orange pulses using the techniques of SFG XFROG [12].

Chapter 5

Crosslinking Experiments

As stated in the introduction to this thesis, this project was began because of interest in using the laser in our lab to perform photochemical crosslinking of DNA to DNA-binding proteins as a step in molecular genetics experiments studying the initiation of DNA replication in human cells. The exact nature of our ultrafast, amplified laser beam made this project unique to our knowledge, and thus exciting. But this also made the project somewhat risky since its results would be of interest to the general research community only if the procedure worked very well as a tool for the biological experiments it was meant to serve, and not in and of themselves.

Significant amounts of time and effort were spent in developing the measurement and analysis procedures necessary to quantify the desired effects, and in optimizing the laser parameters and exposure setup and procedures for achieving the best possible results. A reasonable amount of success has been reached towards the original goal of developing a system and procedure that produces results useful for furthering the larger molecular genetics objectives. It must be noted though that the performance goals as they were

originally stated have not yet been met, and it is unclear whether the current exposure procedure will be of use to the larger experiments, which themselves have not yet been undertaken, nor completely defined. Looking at the experimental data that we have so far obtained, we are able to speculate as to what the limitations of our system are. These speculations will be tested in experiments that are currently being planned.

5.1 Motivation

In eukaryotic cells, the replication of DNA is mediated by a large number of proteins that interact with the DNA in many different ways. The cell cycle-regulated initiation of DNA replication in all eukaryotic organisms involves a multisubunit protein complex termed the origin recognition complex (ORC). Although the budding yeast ORC binds site-specifically to origin DNA, it is not clear if this property is shared by the human ORC. Similarly, it is not known if human ORC must contact the DNA in order to function. The Epstein-Barr virus (EBV) latent cycle origin of DNA replication termed oriP offers a unique opportunity to examine the targeting of human ORC to a defined origin. A single sequence-specific DNA binding protein encoded by the EBV genome, the EBV nuclear antigen-1 (EBNA-1), is required for replication to initiate within oriP. It has been recently determined that a pair of EBNA-1 binding sites from the replicator element of oriP is sufficient to recruit ORC in vivo.

One approach to determine if human ORC makes direct contact with DNA within oriP is to induce the formation of covalent protein-DNA bonds

in living cells and then ask whether ORC is crosslinked to oriP DNA. Traditional ways of forming these covalent DNA-protein bonds include chemical crosslinking with formaldehyde and photochemically induced crosslinking with UV light produced using a lamp. Both methods are problematic for the purpose of characterizing the molecular interaction of ORC with oriP. Formaldehyde induces protein-protein crosslinks, in addition to protein-DNA crosslinks, and cannot distinguish between a direct and indirect (i.e., protein-mediated) interaction of ORC with oriP. Photocrosslinking with a UV lamp is extremely inefficient, generates heat that can adversely affect living cells, and cannot capture transient protein-DNA associations.

Using pulsed UV lasers solves some of these problems. Crosslinking with these powerful UV pulses occurs quickly, sometimes even in one pulse, which does not allow changes to take place in the system before crosslinking occurs [10]. Also, more selectivity for the desired crosslinking reactions over the undesired damage reactions has been observed [14].

The specific results that indicated the possible utility of our laser system (see beginning of Chapter 3) were detailed in [14]. In this work, irradiation of a specific protein-DNA complex with equivalent doses (total energy delivered) of UV pulses of nanosecond, picosecond, and femtosecond length were compared. An absolute crosslinking yield (ACY) was defined which reflected the total percentage of DNA-protein complexes that were crosslinked after an exposure, and it was shown that the femtosecond pulses produced an ACY that was several times that of the picosecond pulses, which in turn produced an ACY that was several times that of the nanosecond pulses. This indicated

that shorter pulses tended to be better at crosslinking than longer pulses. An effective crosslinking yield (ECY) was defined which consisted of the ACY multiplied by the amount of undamaged DNA after an exposure. This quantity was seen to increase as pulse length decreased, further indicating that shorter pulses were most optimal. Finally, in this work exposures were performed in which blue pulses were added to the UV pulses. This was seen to have a significant positive effect on the ECY that was itself dependent on the delay between the UV and blue pulses. A theory that describes the basics of the crosslinking reaction and that predicts the utility of adding blue pulses was described in [14], and will be briefly restated in section 5.1.1.

The specifics of the exposure scheme that produced the best results in the work described above are as follows. The UV and blue femtosecond length pulses were produced with an *unamplified* Ti:Sapphire laser oscillator with a repetition rate of 82 MHz, and the UV pulses were 200 fs long with energies of 0.25 nJ. The blue pulse energy was 1 nJ, and the maximum observed ECE of 14 % occurred at a UV-to-blue delay of 300 fs. The UV dose of the exposure was 0.25 J, so the exposure took place over ≈ 12 seconds.

The general trend of shorter pulses producing a higher ECY indicated that our laser might be useful for this crosslinking. We were able to produce 30 fs pulses as opposed to 200 fs pulses, and theorized that this might not only allow us to improve upon the given value of ECY, but would also allow us to explore the UV-blue delay dependance with greater resolution and accuracy. The important difference between our laser and the one detailed in [14] is the difference in intensity and repetition rate; the power available in our red

beam is comparable. It was unknown what effect this far lower repetition rate and higher pulse intensity would have on the crosslinking results.

5.1.1 Photochemical crosslinking mechanism: theory

As stated above, it was found in [14] that DNA-protein exposure with a beam combining UV *and* blue pulses resulted in an effective crosslinking yield that was significantly (greater than two-fold) greater than that achievable using UV pulses alone. Since this result was a uniquely significant factor in motivating the construction of a bichromatic pump-probe apparatus instead of a far simpler monochromatic sample exposure device, a short description of the theory that has been developed [15, 14] to elucidate the utility of the bichromatic scheme will be given.

Figure 5.1 is a simplified level diagram of a DNA base, which is the primary molecule that absorbs UV light and leads to crosslinking. The molecule can only be promoted from the ground state to the excited state S_1 by a UV photon, which explains why it has never been seen that blue photons alone cause crosslinking to occur. From S_1, the molecule can be ionized with a UV or blue photon, or will eventually transition to a lower energy state through several different pathways. A certain percentage of molecules in the S_1 state will transition to the triplet excited state T_1, which has a relative long lifetime. In the T_1 state, the molecule can again either be ionized with a UV or blue photon or will transition to lower energy states.

DNA-protein crosslinking is only initiated when the DNA base is ionized, yet chemical reactions that lead to DNA damage can be initiated when the

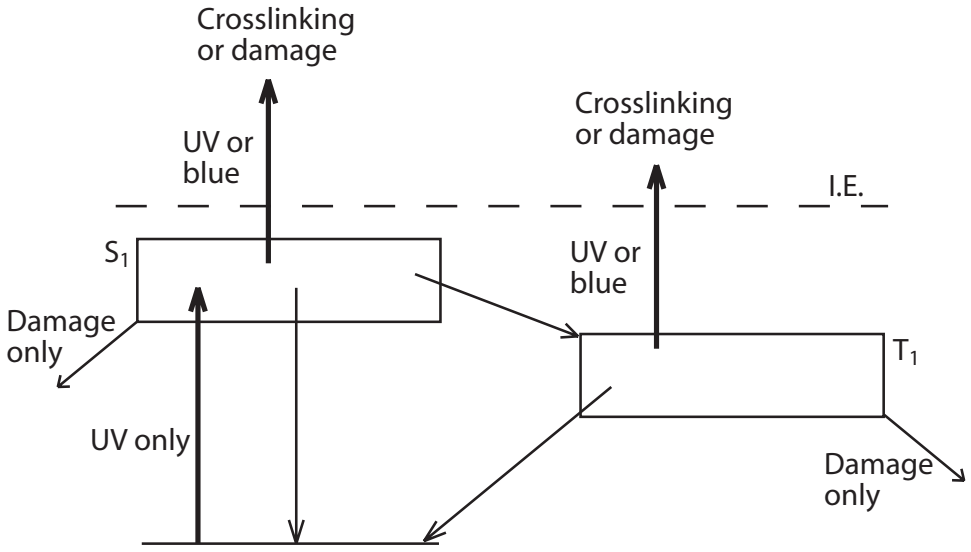

Figure 5.1: Simplified energy level diagram of DNA base involved in photochemical crosslinking. Bold arrows indicate absorption of photons and light arrows indicate transitions to lower energy states either through chemical pathways or through fluorescence. S_1–singlet excited state, T_1–triplet excited state, I.E.–ionization energy.

molecule is either ionized or in one of the excited states S_1 or T_1. This leads to the conclusion that crosslinking with UV and blue light together is better than crosslinking with UV light alone. In the UV-UV crosslinking process, the UV photons which must be present to ionize the molecule after the first UV photon has been absorbed also have some chance to promote more molecules to the S_1 and T_1 states, from which DNA damage can occur. In the UV-blue crosslinking scheme, the blue photons that must be present for ionization can *only* ionize molecules. Thus, it's possible that adding blue light in an exposure could increase ECY over adding UV light of a similar intensity. Calculating exactly how much this increase should be requires a detailed analysis of the molecular model, taking into account all transition

rates and light absorption cross sections that are relevant. This work was done in reference [14], in which results from a more complex version of this model were seen to agree with crosslinking data. It is not known how many of the parameters of the model were set based on previous research, and how many were varied to fit the crosslinking data observed (at least one parameter of the model was said to be measured by these results).

5.2 Methods and procedure

Doing an experiment to determine the effective crosslinking caused by exposure with different sample and laser parameters was a multi-step process that took two people most of a day to complete. The methods and procedure of the experiments will be briefly described here, with emphasis on the laser- and exposure-oriented methods at the expense of the molecular genetics preparation and analysis methods. These latter steps were performed in a separate laboratory.

This experiment uses the collinear UV and blue pulsed beams that were produced by the NLF and BPPI devices detailed in Chapter 3. Except for special cases, which will be noted below, the UV pulses at the entrance to the sample holder had energies of $1-4$ μJ, and lengths of $40-80$ fs (these lengths reflect the shortest and longest values for $\Delta\tau_{\mathrm{XC}}$ that were measured before exposures occurred). For the blue beam, the pulse energy was $15-25$ μJ and the pulse length was similar.

5.2.1 The effective crosslinking efficiency measurement

Because it will be useful for understanding the other methods and procedures, the basic measurements that are done on the samples after exposure will be described first. One is the percentage of DNA in a sample that has been crosslinked to one or more molecules of EBNA-1 by an exposure, and it is called the absolute crosslinking efficiency (ACE)[1]. The other is the percentage of undamaged DNA that is in a sample after exposure, which we label V_P. This stands for "PCR-valid", for reasons that will be seen.

Samples were denatured with an ionic detergent and heat following exposure to the beam and the absolute crosslinking efficiency was measured using gel electrophoresis. This is basically a chromatographic technique that separates molecules by size and shape by placing a voltage across a polyacrylamide gel in which the molecules are allowed to migrate for long period of time (two to three hours). This procedure allowed us to separate DNA that was not covalently linked to EBNA-1 from DNA that was successfully crosslinked to the protein. The DNA that was in each category afterwards could be quantitatively measured because it was tagged previously with ^{32}P, which could then be read by exposing the gels to phosphor storage screens. After several days exposure, the screens were scanned by a phosphorimager and the amount of radioactivity associated with the free and crosslinked DNAs was quantified. There were several control and normalization techniques used in the detailed analysis of this data, but they will not be discussed here.

[1]The name ACE instead of ACY was chosen for this quantity to avoid confusion with a similar measurement performed in [14]. The two quantities should be similar, but are not measured in exactly the same way.

The specific manifestation of DNA damage that was expected to occur upon exposure was that of unwanted crosslinks between bases within DNA strands (pyrimidine dimers). The measurement of this DNA damage was done using quantitative PCR analysis. PCR, of course, stands for polymerase chain reaction, and is the standard laboratory technique by which very small amounts of DNA can be replicated exponentially to make many copies of the same DNA sequence. Quantitative PCR refers to a technique in which the amount of DNA is measured after each doubling step in the replication process using fluorescence, and this measurement is used to project the total amount of DNA at the beginning of the PCR reaction with high accuracy. This technique was used to determine the total amount of DNA that was recovered after an exposure that could be replicated using the PCR process. In order for the DNA to be PCR valid, it had to be *completely* undamaged within the 362 bp sequence amplified by the plasmid-specific primers (that is it could have no inter-DNA crosslinks). The final measurement, V_P, is the amount of PCR-valid DNA as a percentage of the PCR-valid DNA that was recovered from an unexposed sample. In general V_P was more noisy than ACE because it was in essence a measurement of the absolute amount of valid DNA recovered from each exposed sample, as opposed to the relative measurement of the ACE, and thus depended on the ability to recover the same volume of sample after each exposure.

The ACE and V_P measurements were performed on *separate* samples which were exposed under the same conditions. This doubled the amount of samples that had to be exposed on any given exposure run, but was neces-

sary for two reason. First, radioactive DNA could not be used with the PCR process in the laboratory because of the risk of contaminating the thermocycler, and second, with the technique that we used, crosslinked DNA would be reported as "damaged" because it could no longer be replicated using PCR.

The final and most important measurement is called the effective crosslinking efficiency (ECE), and it is simply calculated by $\mathrm{ECE} = \mathrm{ACE} \cdot V_P$. This is the measurement of the percentage of DNA that one would expect after an exposure to be both crosslinked to one or more proteins, and not damaged otherwise. Maximizing this value was the overall purpose of the optimization experiments.

5.2.2 Liquid phase exposure setup

One of the most surprisingly challenging aspects of the crosslinking optimization was the design of the sample holder for exposure. There were many constraints for this subsystem, and some were physically obvious while others, *e.g.* the behavior of the liquid sample in holders of various shapes, required trial and error to detect and correct. The constraints faced, and solution found for them will be reported.

Since the delay between the UV and blue pulses τ was an important parameter in this experiment, it was necessary that this delay be well defined within the interaction region—the UV and protein mix in solution. The first obstacle to this was that dispersive material often necessarily lay between the beam and the sample. Material of any appreciable length, such as a fused silica window or lens, changed τ due to the group velocity mismatch

(GVM, eq. 3.1) in the material. For fused silica, GVM for these wavelengths is 329 fs/mm. The straightforward solution to this problem was to ensure that whatever material was placed in front of the sample during exposure was also placed in front of the BBO_{DFG} crystal before the point of maximum pulse overlap (τ_0) was found. If this material was a lens, then this procedure was made slightly more difficult because placing the lens before BBO_{DFG} meant that the beams exiting BBO_{DFG} were then either focusing or diverging. However, finding τ_0 was still possible in these situations.

The next obstacle to having a well defined value of τ within the sample was the GVM of the blue and UV pulses in water. This was measured to be 330 fs/mm by using the DFXC apparatus to find τ_0 before and after adding 1 cm of water to the beam path. It was also calculated using highly accurate data from [16] to be 360 fs/mm. Since it was desired to achieve a τ resolution of < 100 fs with our setup, this large value of GVM implied that our sample-beam interaction length (L_I, defined as the length along the beam propagation direction in which the sample was illuminated by the beam during exposure) had to be on the order of a few tenths of a millimeter. We did not quite achieve this goal, but we limited L_I as much as possible.

One point that should be made about this water GVM is that [14], which was relied upon as a guide for achieving good exposure results, did not mention this effect at all, and did not state the value of L_I for their setup. In fact, the information that they do give concerning their exposure, which consists of a detailed drawing of the apparatus, seems to indicate that their interaction length is several millimeters long. This is a discrepancy that needs to

be clarified before drawing the final conclusions of this project.

The second important constraint for the sample exposure concerned the problem of non-uniform exposure of sample to light intensity. This was problematic because, as they were done, measurements of ACE and V_P did not measure the same pieces of DNA. To clarify, it was not possible to show that a specific piece of DNA that was crosslinked to a protein was otherwise undamaged. If the sample is exposed to a uniform light intensity, then the crosslinking and damage rates should be the same everywhere within the sample. In this case it would be possible to conjecture that the percentage of DNA that is undammaged and crosslinked can be calculated by multiplying the ACE and V_P together. If the sample is not exposed to a uniform light intensity, however, then this simple multiplication doesn't work. One can imagine an extreme scenario in which only a part of the sample (say 50%) sees UV and blue light at all. In this case, one could imagine irradiating the sample until nearly 100% of the exposed sample becomes crosslinked, and then the ACE for the total sample would be $\approx 50\%$. The value of V_P though could not be less that 50%, even though it might be true that very nearly all of the DNA that was exposed to light was severely damaged. So, one would measure ECE = 25% in this case, even though in reality it is very close to zero.

The first order solution to this problem is to expose the sample to a small area of the beam, across which the beam intensity varies little. One way to do this is to expand the beam with a lens upstream of the samples, and another is to reduce the size of the cross sectional area (A_C) of the sample itself.

Early experiments with expanding the beam gave poor results, which were attributed to the decreased light intensity that resulted from the expansion, so making A_C in addition to L_I as small as possible became a priority.

One other consequence of this flat intensity profile constraint is that the shape of the interface between the light and sample be flat, or very nearly flat. Having the beam enter the sample as a droplet, for example, would not work because the beam would be strongly focused by the curvature of the drop, and its area and intensity would change quickly throughout the sample.

Again, it is unclear how the problem of uneven exposure intensity was handled in reference [14]. The information available on the exposure procedure used indicates that the UV beam was focused by a lens into the sample volume, which itself looks to have an area A_C that is presumably several square millimeters. If this is indeed the case, and there was no attempt made to scan or stir the sample in order to ensure even exposure (neither were mentioned), then one would expect the results of [14] to be faulty. Again, clarification of the exposure procedures used for this work are necessary before final conclusion about it and this work can be drawn.

One last constraint for the sample exposure system was that the sample be easily loaded and recovered. This becomes especially problematic after the first two constraints are satisfied, because if A_C and L_I are both minimized, then the volume of the exposed sample $V = A_C L_I$ must become small as well. Making this more more difficult was the ever present cost constraint, which ruled out the use of expensive sample holders that are designed for similar use—exposing small samples to UV light. All sample holders had

to be disposable, or else hold many samples at once, because cleaning the sample holder between exposures during an exposure run would have been far too time consuming (especially considering that half of the samples were radioactive, and thus had to be handled very carefully!).

The final, and best exposure scheme that we put into use consists of a disposable, yet precisely made capillary tube held horizontally, with a fused silica window (in this case, a fused silica microscope slide) held flat against the opening of the capillary. This exposure scheme is illustrated in Fig. 5.2. Capillaries used had an internal diameter of 0.8 mm, which was probably near the FWHM diameter of the UV/blue beam, although the latter quantity was not measured. Assuming a UV/blue beam diameter of 0.8 mm (in reality, the diameter of the two frequency components would be different), then this sample exposure geometry ensured that all of the sample was exposed to intensities of light greater than or equal to 1/2 the maximum intensity of the beam.

Loading the sample was easy; it was placed at the interface between the slide and capillary using a pipette, and capillary action (appropriately enough) pulled the sample inside to the position shown. Recovery was accomplished by simply removing the capillary from the slide and then expelling the sample and rinsing the capillary using a rubber tube attached to the other end. Aligning the beam into the capillary was also easy. The UV beam was absorbed by the material of the capillary because it was made of a standard, non-UV-transparent glass. Therefore, the UV spot could be easily seen as fluorescence on the front, circular edge of the capillary tube. The tube was

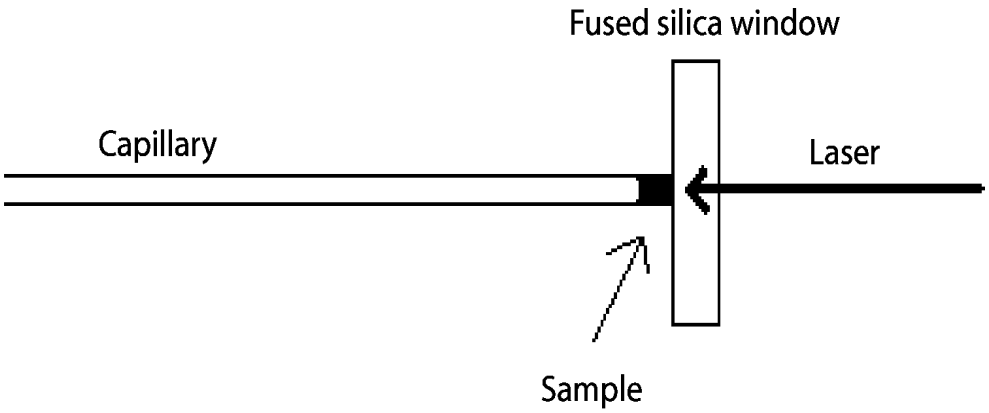

Figure 5.2: Exposure setup for liquid sample. "UV transmissive slab" is in practise a fused silica microscope slide. Capillary tube is in fact open at both ends, as opposed to open at only one end, as shown.

mounted on an xy-stage, and it was moved while looking at the UV spot until the spot was contained within the capillary opening and the minimum amount of fluorescence could be seen on the circular edge.

5.2.3 Exposure procedure

The details of the exposure procedure are in general not important for the analysis of these crosslinking experiments, and would be more appropriately placed as an internal memorandum for those who might be interested in continuing the experiments at a later date. For the purposes of this thesis, it will suffice to say that the exposures were done in sets of 5-20 sample pairs during a day, with the upper limit being set by the number of samples that could be placed in the gel electrophoresis setup at once. These 5-20 sample pairs consisted of one sample to measure ACE and one sample to measure V_P each, and each sample pair was exposed under the same conditions. Post

processing of the samples, measurement of the necessary quantities, and data analysis to determine ACE and V_P values took a day or two after the exposure to complete, so the turn around time between exposures has not quick. A few results of these exposures will be discussed below.

5.3 Results

A total of 21 exposure runs were completed over one year of time, and several general results can be seen in these exposure data.

1. The first, and most robust, result is that blue pulses alone can not perform crosslinking. This was near-universally seen, and any exceptions were not reproducible.

2. In the case of constant pulse energy and length, ACE is proportional to exposure time "T" for small values of ACE, but this relationship rolls off for larger T values. What constitute "large" and "small" values are dependant on the specific exposure situation. An example of data of this type is shown in Fig. 5.3. For this data, the UV pulse energy was 2.2 ± 0.1 μJ and *no* blue pulses were used. For the capillary sample holders, values of ACE above 70% were seen, but for other exposure schemes, ACE was seen to begin saturating at lower levels. A particularly low value at which saturation was seen to occur during one exposure run ($\sim$ 10%) was probably due to the fact that for the particular sample exposure geometry used, only a small percentage of the sample was exposed to the most intense part of the laser beam.

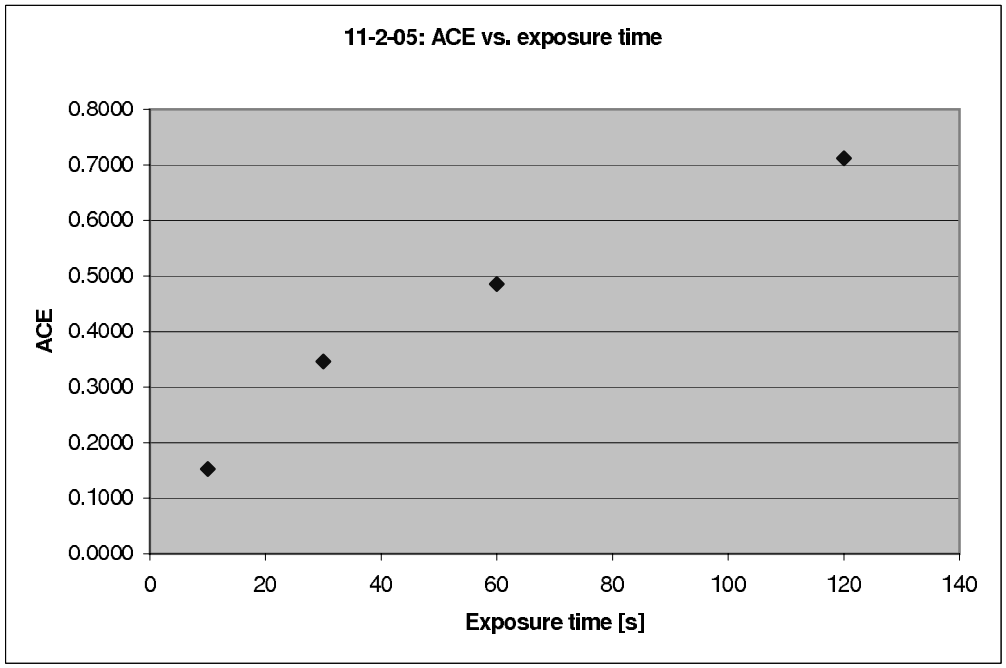

Figure 5.3: Graph of ACE vs. T [s] for exposure in capillaries.

3. The amount of crosslinking that we have achieved per UV dose given to the samples is better than that reported in [14]. As an example of our results, with a repetition rate of 1 kHz and a UV pulse energy of 2.2 ± 1 μJ, an absolute crosslinking efficiency of 35 % was achieved in 30 seconds, which corresponds to a UV dosage of 66 mJ. In reference [14], a similar ACY of $\approx$ 30% was achieved with a UV dosage of 3 J. This is a 50 fold difference in applied energy for a similar crosslinking yield.

4. We observed large amounts of DNA damage corresponding to all appreciable crosslinking yields. Observed values of V_P tended to be on the order of 0.1 %, with values of over 1 % being seen for very short

exposures ($\sim$ 10 s). For the exposure detailed in the previous item in which ACE was equal to 35 %, $V_P = 0.6\%$. Since our values of V_P are so small, it's possible that, for many exposures, practically *all* of the PCR valid DNA that remained was DNA that never saw the UV light, such as DNA that adhered to the outside of the capillary tube.

These low values of V_P are in dramatic opposition to the values of V_P that were reported in [14]. In this work, values of presumably at least 10-20 % were observed for PCR valid DNA while crosslinking efficiencies were very high. A maximum value of 14 % for ECY was reported. As a result of our poor values for V_P, our measured values of ECE have never risen above 1 %.

5. Within the statistical and systematic noise in our experiments, the data comparing UV plus blue exposures with UV alone exposures indicated that blue did not increase ACE or ECE for our specific exposure characteristics. There were only a few indications that this was not the case, but they were in general small and not reproducible. Note that three exposure runs were completed in which many exposures were performed while scanning the UV-blue delay from -700 to 1400 ps. Although these runs had occasional outlier points (including one isolated point that lay several standard deviations away from the rest at a delay of 600 fs), we were not able to observe in these runs any significant dependance of ACE or V_P on UV-blue delay.

5.4 Conclusions and Discussion

We have successfully demonstrated the ability to crosslink DNA to DNA-binding proteins using ultraviolet laser pulses that are < 100 fs in length and have energies of $1 - 3$ μJ. The ACE/dose values that we have seen for UV light alone appear to be quite large. Unfortunately, the DNA damage that we induce when performing such crosslinking is high, and we have not observed that the addition of blue light pulses, at any value of UV-blue delay, improves this situation.

The reasons for these differences between our work and the work detailed in, e.g. reference [14], can probably be traced to the most obvious difference between our exposure setups. We are using an amplified laser beam, and the intensity of our UV pulses is five orders of magnitude larger than the UV pulses that are available with unamplified systems. One speculation that can be made, with reference to the discussion in section 5.1.1, is that blue light makes no difference for our crosslinking because our UV light is so intense that most DNA bases are ionized immediately after being promoted to the excited state S_1. Thus, no molecules are left in that state to await ionization with blue light. One would expect that if this were true, and if it were also true that the previous discussion of the level diagram model were all one needed to know about the system, then this high UV intensity would also lead to high ECE values as well. We have not observed this, and speculate that our high UV intensity might open up new mechanisms for DNA damage that were not previously considered. One recent suggestion[2], was that the

[2]Chris Jacobsen, personal communication.

high UV intensity might be causing the formation of OH^- radicals from ionization of the water itself. These hydroxyl radicals might be responsible for some of the observed DNA damage. New experiments are being planned which will illuminate some of these issues, with the intent still to produce the largest possible values of ECE with the most convenient exposure procedures possible.

Bibliography

[1] P. Agostini and L.F. Dimauro, *The physics of attosecond light pulses*, Rep. Prog. Phys. **67** (2004), no. 6, 813–855.

[2] Sterling Backus, Charles G. Durfee III, Margaret M. Murnane, and Henry C. Kapteyn, *High power ultrafast lasers*, Review of Scientific Instruments **69** (1998), no. 3, 1207–1223.

[3] Robert W. Boyd, *Nonlinear optics*, Academic Press, San Diego, 2002.

[4] Thomas Brabec and Ferenc Krausz, *Intense few-cycle laser fields: Frontiers of nonlinear optics*, Rev. Mod. Phys **72** (2000), no. 2, 545.

[5] R. L. Fork, O. E. Martinez, and J. P. Gordon, *Negative dispersion using pairs of prisms*, Opt. Lett. **9** (1984), 150.

[6] Eugene Hecht, *Optics*, fourth ed., Addison Wesley, 2002.

[7] Takayoshi Kobayashi and Andrius Baltuska, *Sub-5 fs pulse generation from a noncollinear optical parametric amplifier*, Meas. Sci. Technol. **13** (2002), 1671–1682.

[8] Florian Langhojer, David Cardoza, Mark Baertschy, and Thomas Weinacht, *Gaining mechanistic insight from closed loop learning con-*

trol: The importance of basis in searching the phase space, J. Chem. Phys. **122** (2005), 014102.

[9] Ming Li, John P. Nibarger, Chunlei Guo, and George N. Gibson, *Dispersion-free transient-grating frequency-resolved optical gating*, App. Opt. **38** (1999), no. 24, 5250–5253.

[10] Tom Moss, Stefan I. Dimitrov, and Daniel Houde, *Uv-laser crosslinking of proteins to dna*, Methods: Comp. Meth. Enzym. **11** (1997), 225–234.

[11] Patrick Henning Nurnberger and Thomas Weinacht, *Design and construction of an apparatus for the neutral dissociation and ionization of molecules in an intense laser field*, Master's thesis, Stony Brook University, 2003.

[12] D. T. Reid, P. Loza-Alvarez, C. T. A. Brown, T. Beddard, and W. Sibbett, *Amplitude and phase measurement of mid-infrared femtosecond pulses by using cross-correlation frequency-resolved optical gating*, Opt. Lett. **25** (2000), no. 19, 1478.

[13] Derryck T. Reid, *Few cycle EM pulses*, Contemporary Physics **40** (1999), no. 3, 193–204.

[14] Ch. Russmann, J. Stollhof, C. Weiss, R. Beigang, and M. Beato, *Two wavelength femtosecond laser induced DNA-protein crosslinking*, Nuc. Acids Res. **26** (1998), 3967–3970.

[15] Christoph Russmann, Mathias Truss, Andreas Fix, Christian Naumer, Thomas Herrmann, Jochen Schmitt, Jürgen Stollhof, Rene Beigang,

and Miguel Beato, *Crosslinking of pregesterone receptor to DNA using tuneable nanosecond, picosecond and femtosecond UV laser pulses*, Nuc. Acids Res. **25** (1997), no. 12, 2478–2484.

[16] P. Schiebener, J. Straub, J. M. H. Levelt Sengers, and J. S. Gallagher, *Refractive index of water and steam as function of wavelength, temperature and density*, J. Phys. Chem. Ref. Data **19** (1990), no. 3, 677–715.

[17] B. Schmidt, M. Hacker, G. Stobrawa, and T.Feurer, *Lab2—a virtual femtosecond laser lab*, 2004, http://www.lab2.de.

[18] SNLO nonlinear optics code available from A. V. Smith, Sandia National Laboratories, Albuquerque, NM 87185-1423.

[19] C. Trallero-Herrero, D. Cardoza, T. C. Weinacht, and J. L. Cohen, *Coherent control of strong field multiphoton absorption in the presence of dynamic stark shifts*, Phys. Rev. A **71** (2005), 013423.

[20] C. Trallero-Herrero, T. C. Weinacht, and J. L. Cohen, *Strong field atomic phase matching*, Phys. Rev. A (2005), submitted.

[21] Rick Trebino, Kenneth W. DeLong, David N. Fittinghoff, John N. Sweetser, Marco A. Krumbugel, Bruce A. Richman, and Daniel J. Kane, *Measuring ultrashort laser pulses in the time-frequency domain using frequency-resolved optical gating*, Rev. Sci. Instrum. **68** (1997), no. 9, 3277–3295.

[22] Ian Walmsley, Leon Waxer, and Cristophe Dorrer, *The role of dispersion in ultrafast optics*, Rev. Sci. Inst. **72** (2001), no. 1, 1–29.

[23] Shengyi Yang, Kang Lee, Zheng Xu, Xiqing Zhang, and Xurong Xu, *An accurate method to calculate the negative dispersion generated by prism pairs*, Opt. Laser Eng. **36** (2001), 381–387.

[24] Jingyuan Zhang, Aparna Prasad Shreenath, Mark Kimmel, Erik Zeek, Rick Trebino, and Stephan Link, *Measurement of the intensity and phase of attojoule femtosecond light pulses using optical-parametric-amplification cross-correlation frequency-resolved optical gating*, Opt. Express **11** (2003), no. 6, 601–609.